The LEGA-C and SAMI Galaxy Surveys: Quiescent Stellar Populations and the Mass–Size Plane across 6 Gyr

Tania M. Barone[1,2,3,4⋆], Francesco D'Eugenio[5,6], Nicholas Scott[2,4], Matthew Colless[1,4], Sam P. Vaughan[2,3,4], Arjen van der Wel[5], Amelia Fraser-McKelvie[4,7], Anna de Graaff[8], Jesse van de Sande[2,4], Po-Feng Wu (吳柏鋒)[9], Rachel Bezanson[10], Sarah Brough[4,11], Eric Bell[12], Scott M. Croom[2,4], Luca Cortese[4,7], Simon Driver[7], Anna R. Gallazzi[13], Adam Muzzin[14], David Sobral[15], Joss Bland-Hawthorn[2,4], Julia J. Bryant[2,4,16], Michael Goodwin[16], Jon S. Lawrence[17], Nuria P. F. Lorente[17], Matt S. Owers[18,19]

[1]*Research School of Astronomy and Astrophysics, The Australian National University, Canberra, ACT 2611, Australia*
[2]*Sydney Institute for Astronomy, School of Physics, The University of Sydney, NSW, 2006, Australia*
[3]*Centre for Astrophysics and Supercomputing, Swinburne University of Technology, P.O. Box 218, Hawthorn, VIC 3122, Australia*
[4]*ARC Centre of Excellence for All Sky Astrophysics in 3 Dimensions (ASTRO 3D), Australia*
[5]*Sterrenkundig Observatorium, Universiteit Gent, Krijgslaan 281 S9, B-9000 Gent, Belgium*
[6]*Cavendish Laboratory and Kavli Institute for Cosmology, University of Cambridge, Madingley Rise, Cambridge, CB3 0HA, United Kingdom*
[7]*International Centre for Radio Astronomy Research, The University of Western Australia, 35 Stirling Hwy, 6009 Crawley, WA, Australia*
[8]*Leiden Observatory, Leiden University, P.O.Box 9513, NL-2300 AA Leiden, The Netherlands*
[9]*Academia Sinica Institute of Astronomy and Astrophysics, No. 1, Section 4, Roosevelt Road, Taipei 10617, Taiwan*
[10]*Department of Physics and Astronomy and PITT PACC, University of Pittsburgh, Pittsburgh, PA 15260, USA*
[11]*School of Physics, University of New South Wales, NSW 2052, Australia*
[12]*Department of Astronomy, University of Michigan, 1085 S. University Ave., Ann Arbor, MI, 48109, USA*
[13]*INAF - Osservatorio Astrofisico di Arcetri, Largo Enrico Fermi 5, I-50125 Firenze, Italy*
[14]*Department of Physics and Astronomy, York University, 4700 Keele St., Toronto, Ontario, M3J 1P3, Canada*
[15]*Department of Physics, Lancaster University, Lancaster LA1 4YB, UK*
[16]*Australian Astronomical Optics - USyd, University of Sydney, NSW 2006, Australia*
[17]*Australian Astronomical Optics - Maquarie, Macquarie University, NSW 2109, Australia*
[18]*Department of Physics and Astronomy, Macquarie University, NSW 2109, Australia*
[19]*Astronomy, Astrophysics and Astrophotonics Research Centre, Macquarie University, Sydney, NSW 2109, Australia*

arXiv:2107.01054v2 [astro-ph.GA] 11 Mar 2022

Accepted XXX. Received YYY; in original form ZZZ

ABSTRACT

We investigate changes in stellar population age and metallicity ([Z/H]) scaling relations for quiescent galaxies from intermediate redshift ($0.60 \leq z \leq 0.76$) using the LEGA-C Survey to low redshift ($0.014 \leq z \leq 0.10$) using the SAMI Galaxy Survey. Specifically, we study how the spatially-integrated global age and metallicity of individual quiescent galaxies vary in the mass–size plane, using the stellar mass M_* and a dynamical mass proxy derived from the virial theorem $M_D \propto \sigma^2 R_e$. We find that, similarly to at low-redshift, the metallicity of quiescent galaxies at $0.60 \leq z \leq 0.76$ closely correlates with M/R_e (a proxy for the gravitational potential or escape velocity), in that galaxies with deeper potential wells are more metal-rich. This supports the hypothesis that the relation arises due to the gravitational potential regulating the retention of metals by determining the escape velocity for metal-rich stellar and supernova ejecta to escape the system and avoid being recycled into later stellar generations. Conversely, we find no correlation between age and surface density (M/R_e^2) at $0.60 \leq z \leq 0.76$, despite this relation being strong at low-redshift. We consider this change in the age–M/R_e^2 relation in the context of the redshift evolution of the star-forming and quiescent mass–size relations, and find our results are consistent with galaxies forming more compactly at higher redshifts and remaining compact throughout their evolution. Furthermore, galaxies appear to quench at a characteristic surface density that decreases with decreasing redshift. The $z \sim 0$ age–M/R_e^2 relation is therefore a result of building up the quiescent and star-forming populations with galaxies that formed at a range of redshifts and therefore a range of surface densities.

Key words: galaxies: evolution – galaxies: fundamental parameters – galaxies: abundances – galaxies: structure – galaxies: stellar content – galaxies: statistics

⋆ E-mail: tbarone@swin.edu.au

© 2021 The Authors

1 INTRODUCTION

A challenge in the field of galaxy evolution is understanding the influence of redshift-dependent Universe conditions; i.e., how does the redshift at which a galaxy formed affect its evolutionary path (its total mass-assembly and star-formation history)? Galaxies observed at $z \sim 0.76$ (nearly 7 Gyr lookback time) are remarkably different to those observed in the present-day Universe (e.g. Stott et al. 2016; van der Wel et al. 2016; Wisnioski et al. 2019). Compared to nearby galaxies at fixed stellar mass, at intermediate redshifts ($z \sim 0.5$–3) galaxies are more compact (Ferguson et al. 2004; Trujillo et al. 2007; Buitrago et al. 2008; Williams et al. 2010; van der Wel et al. 2014; Mowla et al. 2019), more highly star-forming (with a peak in cosmic star formation density at $z \approx 2$; Lilly et al. 1996; Madau et al. 1998; Daddi et al. 2007; Madau & Dickinson 2014), have dynamically hotter turbulent star-forming gas (Förster Schreiber et al. 2006; Weiner et al. 2006; Law et al. 2007; Förster Schreiber et al. 2009; Law et al. 2009; Wright et al. 2009; Wisnioski et al. 2011; Epinat et al. 2012; Swinbank et al. 2012; Kassin et al. 2012; Wisnioski et al. 2015), and higher molecular gas fractions (Tacconi et al. 2010; Daddi et al. 2010; Tacconi et al. 2013; Morokuma-Matsui & Baba 2015), indicating significant evolution over this time period. Crucially, galaxies today will not follow the same evolutionary path over the next 6 Gyr as similarly-massive galaxies that formed 6 Gyr ago (e.g. Barro et al. 2013; Abramson et al. 2016), because the conditions that influence a galaxy's evolutionary path (e.g. the availability of pristine gas, the scale of galaxy clustering) change as the Universe evolves.

The size difference between star-forming and quiescent galaxies is one piece of evidence for this change in evolutionary path. At fixed mass, star-forming galaxies are larger than their quiescent counterparts (Kriek et al. 2009; Williams et al. 2010; Wuyts et al. 2011; van der Wel et al. 2014; Whitaker et al. 2017). While passive disk fading after ceasing star formation does lead to a decrease in effective radius, this process alone is insufficient to explain the size difference between the $z = 0$ star-forming and quiescent populations (Croom et al. 2021b). Therefore, this difference in average size indicates that the star-forming progenitors of present day quiescent galaxies were different to the $z \sim 0$ population of star-forming galaxies, which will instead evolve into extended quiescent galaxies (Barro et al. 2013).

Understanding the redshift dependence of galaxy evolution requires disentangling the evolution of an individual galaxy within a population from the evolution in the average properties of the population as a whole (due to the continual addition of newly formed galaxies with different properties to the extant population). A key method of studying how both individual and populations of galaxies evolve is by analysing their growth in mass and size. An individual star-forming galaxy is expected to evolve along the relation of star-forming galaxies in the mass–size plane (Lilly et al. 1998; Ravindranath et al. 2004; Trujillo et al. 2006; Pezzulli et al. 2015; van Dokkum et al. 2015), while the average size of the population as a whole increases with decreasing redshift due to processes such as mergers (Hopkins et al. 2009; Naab et al. 2009) and "puffing up" due to strong AGN feedback (Fan et al. 2008, 2010), but also new galaxies forming with larger radii (van Dokkum & Franx 2001; Carollo et al. 2013). In other words, star-forming galaxies at both low and intermediate redshifts follow parallel tracks in the mass–size plane (Speagle et al. 2014; van Dokkum et al. 2015), with their starting location in the plane depending on redshift. Therefore, when analysing star-forming galaxies in the mass–size plane at $z \sim 0$, we are observing the combined effect of both the evolution of individual galaxies throughout their lifetimes and the evolution of the population due to the addition of new members and loss of old members (as they quench). We want to disentangle these two effects to understand how the redshift range over which a galaxy formed and evolved influences its evolutionary path. We therefore need to understand how the processes influencing a galaxy may be regulated by the broader conditions of the Universe and how these conditions change with redshift. An important tool to measure the impact of various processes is the analysis of scaling relations, which quantify the link between different galaxy parameters to determine their dependence. Specifically, scaling relations between stellar population parameters and galaxy structure allow us to quantify how processes involved in star-formation and stellar mass assembly interrelate with processes dominating structural and dynamical changes.

Recent studies analysing various stellar population scaling relations have demonstrated a clear dependence of stellar population and star formation history on galaxy size (R_e), at both low and intermediate ($z \sim 0-3$) redshifts (e.g., Bell et al. 2000; Bell & de Jong 2000; Kauffmann et al. 2003; van der Wel et al. 2009). Franx et al. (2008) investigated the dependence of $u-g$ colour (interpreted as a proxy for star-formation history) on stellar mass (M_*) and R_e for a sample spanning $0 < z < 3$. At all redshifts, they showed that M_* alone is not a good predictor of colour (and thus star-formation history), and that the correlations between $u-g$ colour and M_*/R_e^2 or M_*/R_e have less scatter than the relations with M_*. Wake et al. (2012) extended this work at low redshift ($z < 0.11$), showing that $u-r$ colour correlates more strongly with velocity dispersion (σ) than M_*, M_*/R_e^2 or Sérsic index (Sersic 1968). More recently, Díaz-García et al. (2019) used spectral energy distribution fits to optical and near-infrared photometry from ALHAMBRA (Advanced Large, Homogeneous Area Medium Band Redshift Astronomical Survey; Moles et al. 2008), to study how the stellar population properties of quiescent galaxies vary in the mass–size plane up to redshift $z \sim 1$. They found that stellar population properties show a dependence on galaxy mass and size since $z \sim 1$. Furthermore, low-redshift studies by McDermid et al. (2015), Scott et al. (2017) and Li et al. (2018) using spectroscopically-derived stellar population parameters showed that much of the scatter in the age–M_* and metallicity–M_* relations is due to residual trends with galaxy size, in that smaller galaxies at fixed mass are older and more metal rich. This difference in the resulting mean stellar population parameters can be traced back to differences in the star formation histories using simulations. Gupta et al. (2021) used the IllustrisTNG simulations (Pillepich et al. 2018) to track the evolution of extended massive galaxies and found that, compared to their normal-sized counterparts, extended galaxies quench later despite having similar star-formation rates and stellar masses when selected at $z \sim 2$. Furthermore, in addition to a dependence of global stellar population on galaxy structure, studies have also found a dependence *within* galaxies between local stellar population properties and local dynamical and structural parameters (e.g. González Delgado et al. 2014b, 2015; Møller & Christensen 2020; Zibetti et al. 2020), which suggests the global relations arise from local scales (Scott et al. 2009).

Barone et al. (2018, 2020, hereafter B18 and B20 respectively) built on these earlier studies by quantifying this observed dependence on size, and showing how global age and metallicity ([Z/H]) correlate with the galaxy structure: M_*/R_e (a proxy for the gravitational potential, Φ, or escape velocity[1]) and M_*/R_e^2 (stellar mass

[1] As shown by Scott et al. (2009) and Cappellari et al. (2013b), the difference between the escape velocities for the stellar body and the dark matter halo is not large (~0.1 dex), hence we can adopt M_*/R_e as a qualitative but reliable proxy for the potential well depth and escape velocity.)

surface density, Σ) for low-redshift early-type and star-forming galaxies. Specifically, these studies quantified and compared the intrinsic scatter within each relation and any residual trend with galaxy size. Despite using different samples, methods and models, the two studies found the same results in both early-type and star-forming galaxies: the correlations that are the tightest and have the least residual trend with galaxy size are the age–Σ and [Z/H]–M_*/R_e relations. Additionally, D'Eugenio et al. (2018) showed that gas-phase metallicity in star-forming galaxies at low redshift is also more tightly correlated with M_*/R_e than either M_* or Σ.

Based on these results, B18, B20 and D'Eugenio et al. (2018) proposed and discussed various mechanisms that could lead to the [Z/H]–Φ and age–Σ relations. These studies concluded that the [Z/H]–Φ relation is driven by galaxies with low gravitational potentials losing more of their metals because the escape velocity required for metal-rich gas to be expelled by supernova feedback is directly proportional to the depth of the gravitational potential. Given this assumption, there should also exist a correlation between metallicity and gravitational potential at intermediate redshifts, although the slope and scatter of the relation may vary due to changes in the strength of star formation feedback and outflows. As for the age–Σ relation, B20 proposed it results from compact galaxies having formed earlier than their diffuse counterparts, and so the mechanism(s) responsible for determining the size and mass of a galaxy at fixed age depend on redshift. This hypothesis is in agreement with the results of Díaz-García et al. (2019), who found that the formation epoch of quiescent galaxies since $z \sim 1$ shows a strong dependence on size at fixed mass. The age–Σ relation may therefore be less pronounced at intermediate redshifts, as less time has passed for the relation to build up. The aim of this paper is to test these hypotheses, by determining the redshift dependence of the age–Σ and [Z/H]–Φ scaling relations.

In this paper we build on the results of stellar populations scaling relations at low redshift by analysing if (and how) the relations change across a lookback time of 6 Gyr ($0.014 \leq z \leq 0.76$), to test the hypotheses proposed for the age–Σ and [Z/H]–Φ scaling relations. Specifically, we study how the spatially-integrated average (global) age and metallicity of individual quiescent galaxies vary in the mass–size plane, using both the stellar mass M_* and a proxy for the dynamical mass derived from the virial theorem ($M_D \propto \sigma^2 R_e$). Furthermore, we look at how the age–Σ and [Z/H]–Φ relations found at low redshift appear at $0.60 \leq z \leq 0.76$. By quantifying the significance of these scaling relations at low and intermediate redshift we aim to understand their origins and, in the process, begin to discern the redshift dependence of stellar population evolution over the past 6 Gyr.

The paper is arranged as follows. In Section 2 we describe the $0.60 \leq z \leq 0.68$ and $0.68 < z \leq 0.76$ samples from the LEGA-C survey and the $0.014 \leq z \leq 0.10$ comparison sample from the SAMI survey. Section 3 describes the full spectral fitting method used to obtain the metallicity and age measurements, as well as our analysis methods. We present the [Z/H] and age results in Section 4, followed by a discussion in Section 5. In discussing the age results we link the age–Σ relation to the distribution of the quiescent and star-forming populations across redshift in the mass–size plane in Section 5.2.1. Lastly we provide a summary of our conclusions in Section 6. We assume a flat Λ cold dark matter (ΛCDM) Universe with $\Omega_\Lambda = 0.7$, $\Omega_M = 0.3$ and $H_0 = 70\,\mathrm{km\,s^{-1}\,Mpc^{-1}}$, and a Chabrier (2003) initial mass function.

2 DATA

We describe the LEGA-C and SAMI surveys in Sections 2.1 and 2.2 respectively, followed by describing auxiliary parameter measurements in Section 2.3. The adopted quiescent versus star-forming galaxy selection criterion is detailed in Section 2.4.

2.1 The LEGA-C Survey

The Large Early Galaxy Astrophysics Census (LEGA-C; van der Wel et al. 2016) is a slit spectroscopic survey of galaxies at intermediate redshifts in the COSMOS field (Scoville et al. 2007), using the VIsible Multi-Object Spectrograph (VIMOS; Le Fèvre et al. 2003) on the Very Large Telescope. LEGA-C targets were selected from the UltraVISTA catalogue (Muzzin et al. 2013a) based on a redshift-dependent apparent K_S magnitude limit: $K_s < 20.7 - 7.5\log((1+z)/1.8)$ (van der Wel et al. 2016), which has the advantage of closely resembling a selection on stellar mass while remaining model independent (see Appendix A of van der Wel et al. 2021). The survey comprises 4209 galaxies, 3472 of which have spectroscopic redshift measurements within $0.60 \leq z \leq 1.0$. Targets were observed for ~20 hours to reach an approximate S/N per Å ≈ 20 in the continuum. We use integrated spectra summed along the entire slit, with an effective spectral resolution of R~3500 (Straatman et al. 2018) and observed wavelength range ~6300Å–8800Å. We use spectra from the third data release (van der Wel et al. 2021)[2]; see van der Wel et al. (2016) and Straatman et al. (2018) for earlier data releases.

While the LEGA-C sample spans the redshift range $0.60 \leq z \leq 1.0$, above $z \sim 0.8$ the survey selection criteria and the S/N requirement for stellar population analyses (median S/N per Å ≥ 10 in the rest-wavelength region 4427–4548 Å; see Section 2.5) limit the sample to only the brightest (most massive) targets. We therefore restrict our analysis to the redshift range $0.60 \leq z \leq 0.76$. We then estimate the size evolution with redshift for this redshift range using the relations from van der Wel et al. (2014) and Mowla et al. (2019) for high ($\log M_*/M_\odot > 11.3$) and intermediate $\log M_*/M_\odot \sim 10.75$) mass galaxies respectively. To ensure the size evolution is less than 0.05 dex (the uncertainty on the size measurements), we split the sample into two redshift bins: $0.60 \leq z \leq 0.68$ and $0.68 < z \leq 0.76$. Lastly, given the LEGA-C sample at z~ 0.7 is representative down to a stellar mass limit of $\log M_* \geq 10.48$ (van der Wel et al. 2021), we restrict our analysis to LEGA-C galaxies with $10.48 \leq \log M_* \leq 11.5$. This leaves final samples of 412 galaxy (219 quiescent, 193 star-forming) for $0.60 \leq z \leq 0.68$, and 513 (273 quiescent, 240 star-forming) for $0.68 < z \leq 0.76$.

2.2 The SAMI Galaxy Survey

The Sydney-AAO Multi-object Integral-field (SAMI; Bryant et al. 2015; Croom et al. 2021a) Galaxy Survey is a low-redshift integral-field survey of 3068 unique galaxies observed using the SAMI instrument (Croom et al. 2012) connected to the AAOmega spectrograph (Sharp et al. 2006, 2015) on the Anglo-Australian Telescope. The sample spans the redshift range $0.004 \leq z \leq 0.11$. Galaxies were observed through fused-fibre hexabundles (Bland-Hawthorn et al. 2011; Bryant et al. 2014), each comprising 61 tightly-packed fibres

[2] The data can be accessed from http://archive.eso.org/cms/eso-archive-news/Third-and-final-release-of-the-Large-Early-Galaxy-Census-LEGA-C-Spectroscopic-Public-Survey-published.html

that form an approximately circular grid with a diameter of 15". Observations were typically for a total of 3.5 hours comprised of 7 dithers of 30 minutes each. Targets were selected based on stellar mass cuts in narrow redshift bins from three equatorial regions covered by the volume-limited Galaxy And Mass Assembly (GAMA; Driver et al. 2011) survey and 8 cluster regions; see Bryant et al. (2015) and Owers et al. (2017) for a full description of the sample selection for the GAMA and cluster regions respectively. For this analysis we exclude targets from the cluster regions to avoid over-representing galaxies from dense environments (e.g. as discussed in van de Sande et al. 2021), leaving the SAMI-GAMA sample which is highly complete ($\sim$ 90%) for $\log M_* \geq 10$ (Bryant et al. 2015; van de Sande et al. 2021; Croom et al. 2021a). SAMI spectra have two components, a 'blue' component (3700–5700 Å) at a resolution of R=1800, and a 'red' component (6300–7400 Å) at R=4300. For the full-spectral fits the higher spectral resolution red component is degraded to match the resolution of the blue component. The whole spectrum is then fit simultaneously. We use spatially-integrated $1R_e$ spectra from the third data release (Croom et al. 2021a)[3]; see Allen et al. (2015), Green et al. (2018) and Scott et al. (2018) for earlier releases.

As for the LEGA-C samples, we want to ensure the redshift evolution within our SAMI sample is less than the typical uncertainty on the size measurements (0.05 dex). We calculate the estimated size evolution within the SAMI redshift range using the same relations of van der Wel et al. (2014) and Mowla et al. (2019) used in Section 2.1 for the LEGA-C sample. Based on the estimated size evolution, we remove 22 galaxies at the ends of the redshift range. Our final SAMI sample comprises of 974 galaxies (524 quiescent, 450 star-forming) with $10.0 \leq \log M_* \leq 11.5$, median S/N per Å ≥ 10 in the rest wavelength region 4427–4548, and in the redshift range $0.014 \leq z \leq 0.10$.

2.3 Measurements of galaxy properties

Semi-major effective radii (R_e) were measured from Sérsic fits using the GALFIT software (Peng et al. 2010) by van der Wel et al. (2021) for the LEGA-C sample and Hill et al. (2011) for the SAMI sample. For LEGA-C targets van der Wel et al. (2021) followed the procedure of van der Wel et al. (2012) on HST ACS F814W images from the COSMOS program (Scoville et al. 2007). For SAMI targets, Hill et al. (2011) followed the process of Kelvin et al. (2012), using r-band photometry from SDSS DR7 (Abazajian et al. 2009) reprocessed for GAMA. We note that colour gradients within galaxies affect the absolute measurement of R_e, in that bluer bands lead to larger size measurements (e.g. Kelvin et al. 2012). However, given our analysis focuses on the relative difference in size *within* each redshift bin, any systematic offset between the SAMI and LEGA-C size measurements due to the difference in photometric band does not affect our results.

We use stellar masses (M_*) and star formation rates (SFR) measured by de Graaff et al. (2020, 2021) for the LEGA-C galaxies and Driver et al. (2018) for the SAMI galaxies. In both catalogues the measurements were derived using the MAGPHYS (Multi-wavelength Analysis of Galaxy Physical Properties; da Cunha et al. 2008) spectral energy distribution fitting software, based on the Bruzual & Charlot (2003) library of simple stellar population spectra, a Charlot & Fall (2000) dust attenuation model, a Chabrier (2003) initial mass function and an exponentially declining star formation history (however the LEGA-C star formation history also includes random star-formation bursts). While the two catalogues differ slightly in the photometric bands used for the fits due to differences in data availability, they both include photometry ranging from ultra-violet to the far-infrared. Specifically, de Graaff et al. (2021) used ugriz and BVYJHK$_s$ from UltraVISTA as well as Spitzer infrared and multiband (rest-frame mid ultra-violet to far-infrared), while Driver et al. (2018) used FUV, NUV, ugriz, ZYJHK, W1234, PACS100/160 and SPIRE 250/350/500 (rest-frame far ultra-violet to far-infrared). See de Graaff et al. (2021) and Driver et al. (2018) for further details. The samples are complete in stellar mass within each redshift bin ($\log M_* \geq 10, 10.48, 10.48 M_\odot$ for $z_{\rm SAMI} \in [0.014, 0.10]$, $z_{\rm LEGA-C} \in [0.60, 0.68], [0.68, 0.76]$ respectively). Our results are qualitatively unchanged if we use the same stellar mass limit ($\log M_* \geq 10.48$) for all three redshift bins.

We choose to use an independent measure of the stellar mass rather than those derived from the full spectral fits due to the increased wavelength coverage of the MAGPHYS masses. Given the rest spectral range of the LEGA-C ($\sim$3700–5200 Å for $z = 0.67$) and SAMI spectra ($\sim$3500–5400 and 6000–7000 Å for $z = 0.05$), masses derived from the full spectral fits include predominantly blue light, so they will be inevitably biased due to not sampling the rest-frame infrared. MAGPHYS stellar masses are based on a broader wavelength range (rest-frame ultra-violet to far infrared), which contains more

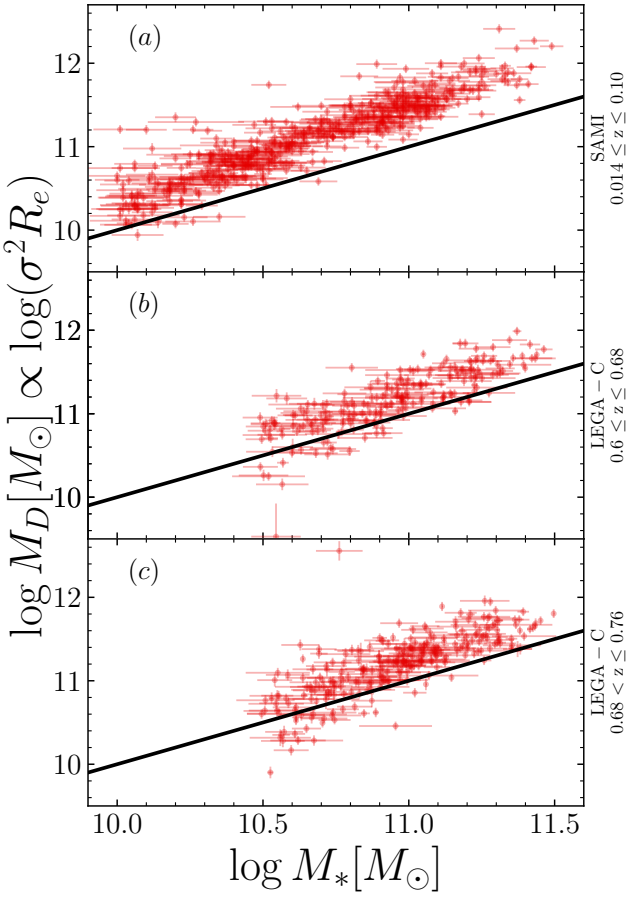


Figure 1. The stellar mass M_* versus the virial proxy for the dynamical mass M_D for the three redshift samples. The solid black line shows the 1-1 relation. Each point shows the 1σ uncertainty on $\log M_*$ and $\log M_D$. There is good agreement between the two mass estimates, with the dynamical masses being 0.4 and 0.2 dex higher for the SAMI and LEGA-C samples respectively.

[3] The data can be accessed at https://docs.datacentral.org.au/sami/

information about dust extinction and reaches redder wavelengths than the spectroscopy alone.

In addition to covering the GAMA regions from which the SAMI sample was selected, the Driver et al. (2018) catalogue also includes measurements for the G10-COSMOS region (Davies et al. 2015; Andrews et al. 2017) which includes 301 LEGA-C galaxies. We use this overlap of 301 galaxies to check for systematic biases between the samples that might arise from the different photometric bands used in the SED fits. We find good agreement between the two catalogues for both the stellar masses and the star formation rates. The mean difference between the two catalogues is 0.08 ± 0.15 dex for $\log M_*$ and 0.07 ± 0.40 dex for log SFR, with the values from de Graaff et al. (2021) being slightly more massive and star-forming.

Lastly we define a simple proxy for the total (dynamical) galaxy mass M_D based on the virial theorem:

$$M_D \equiv k\sigma^2 R_e/G \quad (1)$$

Where σ is the aperture velocity dispersion (measured from the pPXF fits; see Section 3.1), G is the gravitational constant (4.3×10^{-6} km^2 kpc s^{-2} $M_\odot^{-1}$), and k is a constant set to 5.0 (Cappellari et al. 2006). Figure 1 shows the stellar and dynamical mass estimates for the quiescent galaxies in the three redshift bins. In all three redshift samples there is good linear agreement between the stellar and dynamical estimates, with M_D being systematically 0.4 and 0.2 dex more massive than M_* for SAMI and LEGA-C galaxies respectively. We note that the higher $\log M_D - \log M_*$ for SAMI galaxies compared to LEGA-C is likely driven by the smaller physical coverage of the SAMI galaxies ($1R_e$) compared to LEGA-C ($\gtrapprox 1R_e$; see Section 2.5). However, given our analysis focuses on trends within redshift bins, systematic differences between bins does not influence our results. For a detailed discussion and analysis of dynamical versus stellar masses for LEGA-C galaxies, we refer the reader to de Graaff et al. (2021).

2.4 Quiescent Galaxy Selection

We separate quiescent and star-forming galaxies in both the LEGA-C and SAMI samples based on their distance from the redshift-dependent star-forming main sequence defined by Whitaker et al. (2012):

$$\log \mathrm{SFR} = (0.70 - 0.13z)(\log M_* - 10.5) + 0.38 + 1.14z - 0.19z^2 \quad (2)$$

We show this relation in Figure 2 (solid black line) using the central redshift value in each bin ($z = 0.057, 0.64, 0.72$). We do an initial cut 1 dex below the relation and measure the root-mean-square (RMS) scatter about the trend. We then define quiescent galaxies as those with $\mathrm{SFR}_Q < \mathrm{SFR}_{MS} - 2\mathrm{RMS}$ (dotted black line). The precise selection cut for each redshift bin is given in the corresponding panel of Figure 2.

Post-starburst galaxies are a subclass of quiescent galaxies that recently quenched after a burst of star-formation (Dressler & Gunn 1983; Balogh et al. 1999; Dressler et al. 1999), and therefore contain a young average stellar population. As a result of their rapid quenching (Wu et al. 2020), post-starburst galaxies tend to be smaller than the rest of the quiescent population at fixed mass (Whitaker et al. 2012; Yano et al. 2016; Almaini et al. 2017). The young average ages and small sizes of post-starburst galaxies are contrary to the rest of the quiescent population in which young galaxies tend to be larger at fixed mass (Wu et al. 2018). The number of post-starburst galaxies in our three redshift samples (defined as quiescent galaxies with an equivalent width of $H\delta_A > 4$Å; e.g. Wu et al. 2018; D'Eugenio et al. 2020) is 2, 8, and 19 (0.4%, 4%, and 7%) for $0.014 \leq z_{\mathrm{SAMI}} \leq 0.10$,

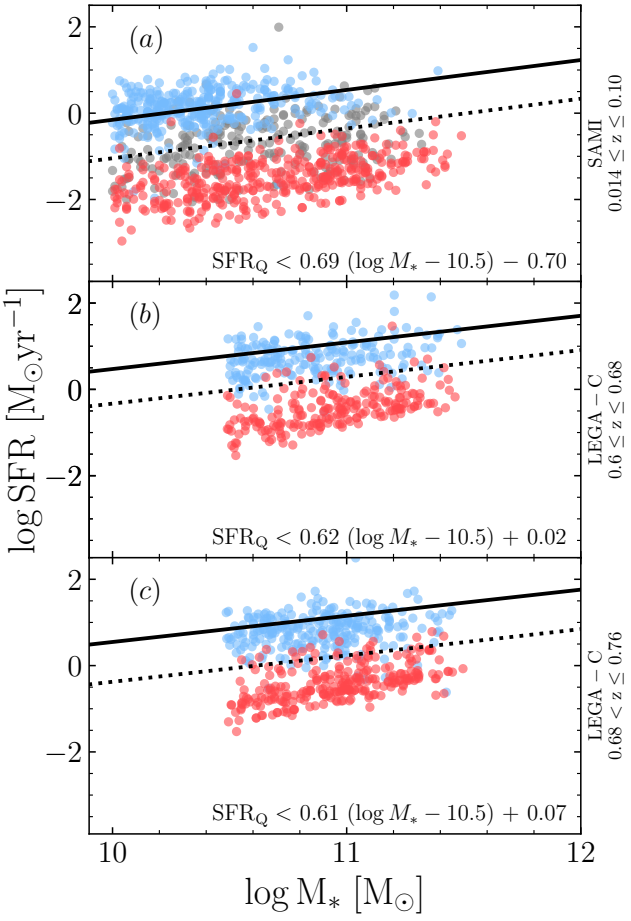


Figure 2. Star formation rate versus stellar mass for the three redshift bins. The black solid lines are the redshift-dependent main sequence from Whitaker et al. (2012, see Equation 2). The dotted black lines are the adopted boundary between quiescent and star-forming galaxies, defined as $\mathrm{SFR}_Q < \mathrm{SFR}_{MS} - 2\mathrm{RMS}$ (bottom right of each panel), where RMS is the measured scatter about the main sequence based on an initial cut 1 dex below the relation. The points are coloured using quiescent (red points), star-forming (blue points), and intermediate (grey points; panel a only) selection criteria from the literature (see Section 2.4.1); our adopted selection criteria are comparable to these alternatives.

$0.60 \leq z_{\mathrm{LEGA-C}} \leq 0.68$ and $0.68 < z_{\mathrm{LEGA-C}} \leq 0.76$ respectively. It can be argued that post-starburst galaxies should be removed from our sample, because their evolutionary path with a final starburst in the centre is different from the rest of the galaxy population (Wu et al. 2018, 2020; D'Eugenio et al. 2020). However, when we repeat our analysis after having removed these galaxies, we find the results qualitatively unchanged. Therefore we do not remove post-starburst galaxies from our quiescent samples.

2.4.1 *Comparison to other Quiescent classifications*

We use the star-forming main sequence as defined by Whitaker et al. (2012) because their analysis used the same cosmological parameters and IMF assumed in this work and covers the full redshift range of both the LEGA-C and SAMI samples. We note however that the Whitaker et al. (2012) results are based on linear fits in the log SFR–log M_* plane, but more recent works have shown that the star-forming

main sequence turns over at high stellar masses (e.g. Leslie et al. 2020). We therefore test our analysis using other quiescent selection criteria used in the literature for the two surveys.

In Figure 2 we compare our quiescent selection criterion to others used in the literature for the two surveys. The SAMI galaxies (panel a) are coloured by the selection used in Croom et al. (2021b), which is based on the star formation rates from Medling et al. (2018) and distance from the Renzini & Peng (2015) main sequence. The LEGA-C galaxies (panels b and c) are coloured by their U–V vs V–J diagram classification (Labbé et al. 2005), as defined by Muzzin et al. (2013b) and used in, e.g., Chauke et al. (2018), Wu et al. (2018) and Straatman et al. (2018). Figure 2 shows that our quiescent selection based on distance from the Whitaker et al. (2012) main sequence is comparable to these alternative selection criteria used in the literature. We repeated our anlysis using these alternate quiescent selection criteria and find our results unchanged. Therefore, we use the quiescent criteria based on the Whitaker et al. (2012) main sequence and MAGPHYS derived SFR and M_* for consistency across the two surveys.

2.5 Survey Comparison

Galaxies have well established internal radial stellar population gradients that, when combined with a varying aperture size, can lead to spurious global trends. A key difference between the two surveys are the apertures used; the VIMOS instrument used by LEGA-C has slits 1" wide and 8" long whereas the SAMI instrument uses fused-fibre hexabundles of 15" diameter, comprised of 61 individual fibres each 1.6" in diameter. For the SAMI targets we use spectra integrated within 1 effective radius (R_e), and for the LEGA-C data we use spectra integrated along the entire slit. At $z = 0.7$ 1" corresponds to a physical scale of ~7.1 kpc which encompasses at least 50% of the total flux, but depending on the galaxy's apparent size the spectrum will also contain flux from outer regions ($R > R_e$). Therefore, despite the different apertures used in the two surveys, all galaxies are probed to at least $1R_e$, mitigating potential aperture bias in measurements between the two surveys. We emphasise, however, that we are not directly comparing stellar population parameters between the redshift bins, rather we are interested in how properties vary *within* redshift bins. Therefore, any systematic bias in stellar population measurements arising from the differences between the two instruments do not influence our analysis.

In Figure 3 we compare the spectral data quality of the quiescent samples between the two surveys by comparing the median spectral S/N per Å in the rest-wavelength range covered by all targets (4427–4548 Å). The median S/N for the three samples are $S/N_{SAMI} = 59$, and $S/N_{LEGA-C} = 39$ and 35 for $z \in [0.60, 0.68]$ and $z \in [0.68, 0.76]$ respectively. The black dotted line shows our adopted quality threshold at S/N ≥ 10. This minimum S/N requirement only affects 5 quiescent galaxies in the highest redshift LEGA-C bin which span in stellar mass from $\log M_* = 10.6$ to $11.3 M_\odot$. We therefore consider the effect of this quality cut on the overall mass-completeness of the sample to be negligible.

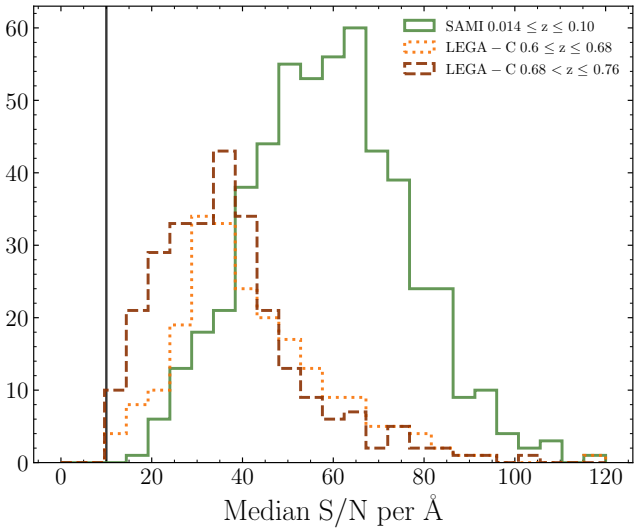


Figure 3. Median spectral S/N per Å in the rest-wavelength region 4427–4548 Å for SAMI (solid green) and LEGA-C ($z \in [0.60, 0.68]$ dotted orange, $z \in [0.68, 0.76]$ dashed brown) quiescent galaxies. The solid black line represents the S/N threshold (S/N≥ 10) of all three redshift samples. The median S/N for the three samples is $S/N_{SAMI} = 59$, and $S/N_{LEGA-C} = 39$ and 35 for $z \in [0.60, 0.68]$ and $z \in [0.68, 0.76]$ respectively.

3 METHODOLOGY

3.1 Stellar Population Measurements

Luminosity-weighted stellar population parameters for both the LEGA-C and SAMI galaxies are measured from full spectral fits using 350 theoretical templates based on the Extended Medium resolution INT Library of Empirical Spectra (E-MILES; Sánchez-Blázquez et al. 2006; Vazdekis et al. 2016), isochrones from Girardi et al. (2000) and a Chabrier (2003) initial mass function. We use the full set of 350 templates which contain 50 age values ranging from 0.063 to 17.78 Gyr, 7 [Z/H] values ranging from −2.32 to +0.22, and have [α/Fe] values scaled to the solar neighbourhood (the "base" models; Vazdekis et al. 2016). The normalisation for the luminosity-weighting is calculated in the range from 3000–8000Å. We tested our analysis using the BaSTI isochrones (Pietrinferni et al. 2004, 2006) and found our results qualitatively unchanged. We fit the templates to the de-redshifted spectra using the Python implementation of the publicly available Penalized Pixel-Fitting software (pPXF; Cappellari & Emsellem 2004; Cappellari 2017). We do an initial fit to ensure that we have a good estimate of the S/N ratio per pixel and multiply the noise by a rescaling coefficient so that the reduced χ^2 is unity. The median rescaling is 1.45 for the LEGA-C sample and 0.54 for the SAMI sample, with standard deviations of 0.31 and 0.21 respectively. We then use this improved estimate of the noise for the second (final) fit. The improved noise estimate is also used to measure the S/N per Å in the rest wavelength range 4427–4548 Å. This wavelength range was chosen because it is covered by all galaxies in the two samples. To account for dust reddening and any offsets to the continuum shape due to flux calibration, this final fit includes a 10^{th} degree multiplicative polynomial.

The final age and metallicity values are the weighted average of all the templates:

$$\log \text{Age} = \frac{\Sigma w_i \log \text{Age}_i}{\Sigma w_i} \tag{3}$$

$$[\text{Z/H}] = \frac{\Sigma w_i [\text{Z/H}]_i}{\Sigma w_i} \tag{4}$$

where w_i is the weight measured from pPXF for the i^{th} template,

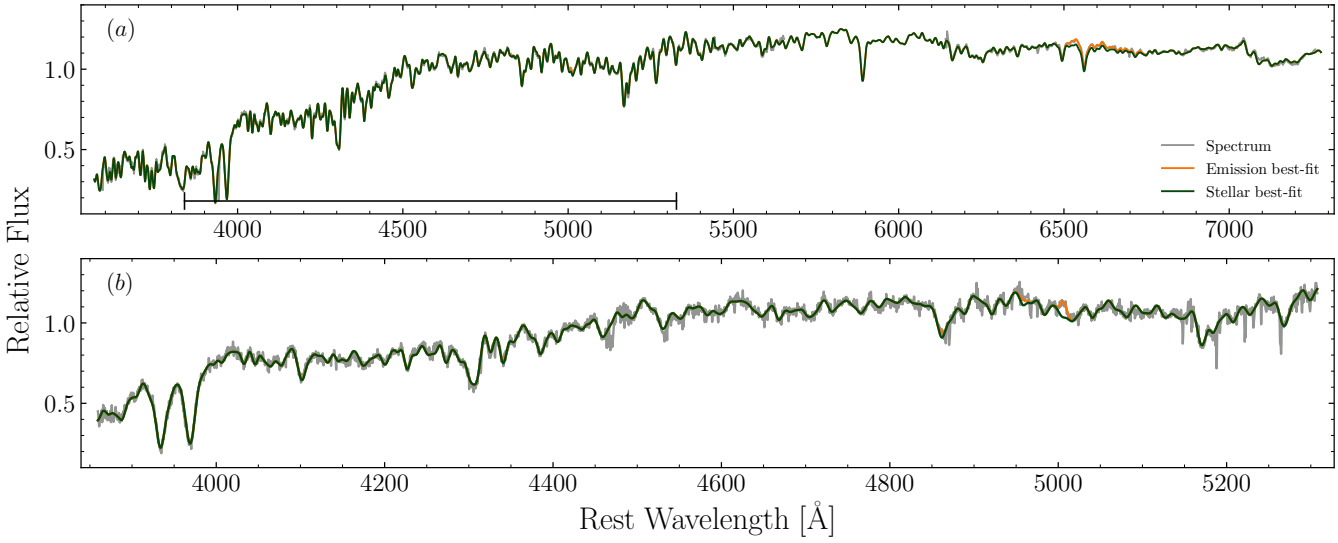


Figure 4. Example full spectral fits for SAMI galaxy ID=278109 (panel a) and LEGA-C galaxy ID=206573, mask ID=1 (panel b). In both panels the original spectrum is shown in grey, with the best-fit from the stellar templates in green and the best-fit emission templates in orange. By simultaneously fitting the stellar and gas components, we are able to recover absorption features masked by emission lines. The black horizontal line in panel a shows the wavelength range of panel b for ease of comparison. The fluxes are normalised such that the median flux across the spectrum is 1.

with single-burst age and metallicity values and $[Z/H]_i$ and age_i. Following McDermid et al. (2015) and González Delgado et al. (2015), the weighted average age is measured using the logarithm of the template ages because the template ages are sampled logarithmically.

All fits are done without linear regularisation, which imposes constraints on the weights of neighbouring templates (in age-metallicty space) to vary smoothly. While using linear regularisation produces more realistic star-formation histories, by construction reasonable degrees of regularisation do not significantly change the weighted average age and [Z/H] values (B20).

In addition to the stellar templates, we also include templates for common gas emission lines. We fix the flux ratios of the Balmer series from H_α to H_θ assuming a decrement based on Case B recombination (electron temperature $T = 10^4$ K and number density $n = 100\,\mathrm{cm}^{-3}$; Dopita & Sutherland 2003), using the TIE_BALMER pPXF keyword. Any residual difference in flux from the fixed ratios is attributed to dust extinction, which is fit using a Calzetti et al. (2000) attenuation curve (via the GAS_REDDENING keyword). We also limit the ratios of the [OII] and [SII] doublets to lie within the theoretical ranges predicted by atomic physics (Osterbrock & Ferland 2006) using the LIMIT_DOUBLETS keyword. The [OIII], [OI] and [NII] doublets also have their flux ratios tied based on atomic physics. We show example fits in Figure 4 for SAMI galaxy ID=278109 and LEGA-C galaxy ID=206573 mask ID=1.

The fits are done using the full wavelength range available for each spectrum; the typical rest-wavelength range for the SAMI and LEGA-C spectra are ~3461–7077 Å and ~3723–5168 Å respectively. We tested the resulting age and metallicity values from fits to SAMI spectra that were restricted to use the rest wavelength range typical of the LEGA-C sample. While we found good agreement for both the age and metallicity values, the age values in the reduced wavelength range were on average 0.067 ± 0.064 dex younger than when fitted using the full SAMI wavelength range. This modest difference is expected given that the wavelength range 3723–5168 Å contains more and stronger stellar absorption features compared to the range 5168–7077 Å. Given we are interested in the age variations *within* each redshift bin, our results and interpretations are not affected by this minor discrepancy.

We check our stellar population measurements by comparing to other studies probing similar redshift ranges. We note that the absolute age of stellar population templates (and thus resulting age measurements) are not well constrained (e.g. McDermid et al. 2015; Scott et al. 2017), therefore, differences in stellar population synthesis methods and models can induce systematic offsets in the absolute age and metallicity value assigned to each galaxy. However the rank order of galaxies relative to each other, and therefore scaling relations, should remain consistent. We find the age–M_* and [Z/H]–M_* relations are consistent in shape across all three redshift bins (with massive galaxies being older and more metal rich), in agreement with the study by Gallazzi et al. (2014) in a similar redshift range. Furthermore, in agreement with Choi et al. (2014), our measurements show negligible evolution in [Z/H] at fixed mass across the three redshift bins.

We estimate uncertainties for the age and metallicity measurements for both the LEGA-C and SAMI samples by randomly shuffling the residuals between the best-fit and the observed spectrum, which are then reassigned to the best-fit spectrum and refit. This process is repeated 100 times per galaxy, building up a distribution of values in age and metallicity. To ensure we preserve any wavelength dependence of the residuals in this process, the residuals are reassigned within wavelength bins approximately 500 Å wide. The distributions are approximately Gaussian and centred around the original fit value, so we take the standard deviations of the distributions as the uncertainties on the original age and metallicity measurements. The median uncertainties in the three redshift bins are $\sigma_{[Z/H]} = 0.03$, 0.07, and 0.07 dex for metallicity (shown in Figures 5 and 6) and $\sigma_{\log \mathrm{Age}} = 0.03$, 0.08, and 0.08 dex for log Age (shown in figures 9 and 10) for $0.014 \leq z_{\mathrm{SAMI}} \leq 0.10$, $0.60 \leq z_{\mathrm{LEGA-C}} \leq 0.68$, and $0.68 < z_{\mathrm{LEGA-C}} \leq 0.76$ respectively.

For both the SAMI and LEGA-C stellar population fits, we allow for the full range of template ages (0.063 to 17.78 Gyr), despite the age of the Universe at $z = 0.76$ being ~ 7 Gyr. This is because the

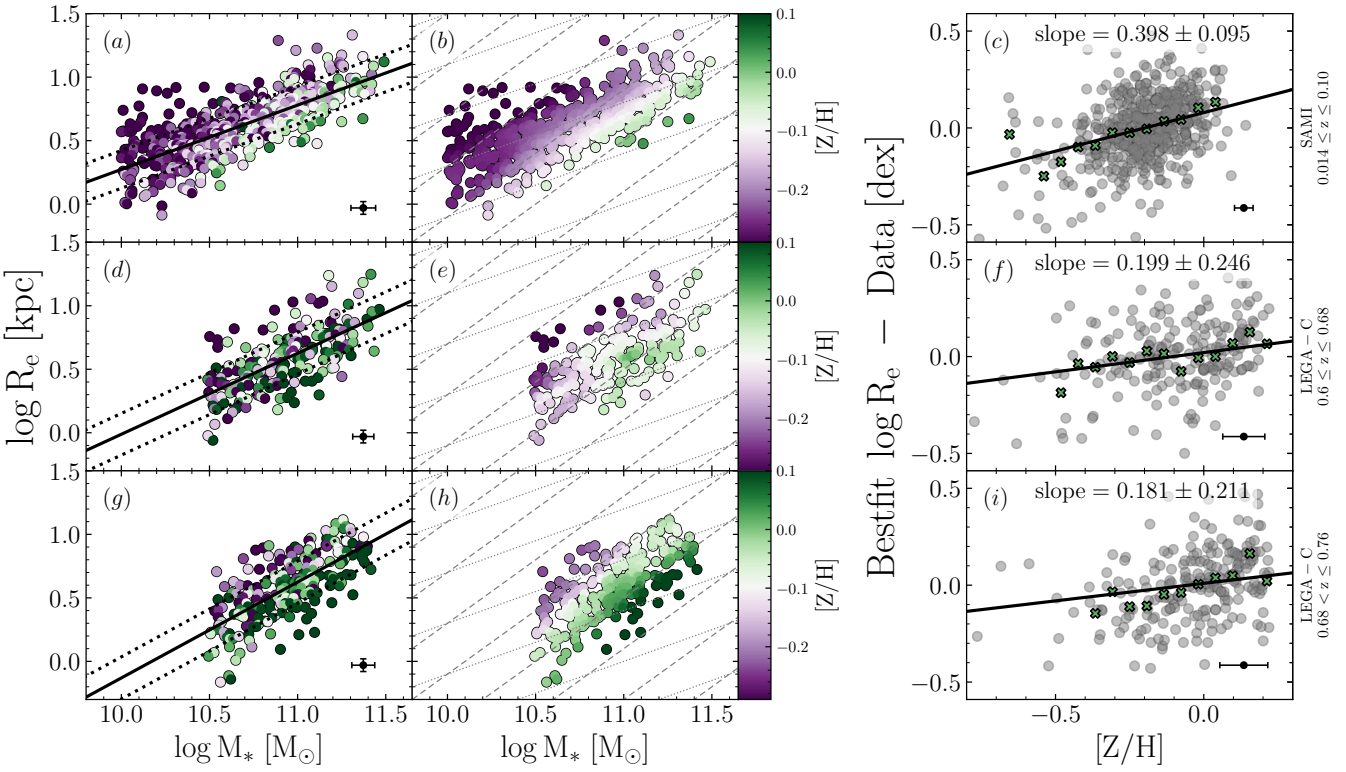


Figure 5. Stellar metallicity [Z/H] of quiescent galaxies in the stellar mass–size plane for three redshift bins. The top row shows the SAMI galaxies $0.014 \leq z \leq 0.10$, middle row the LEGA-C galaxies with $0.60 \leq z \leq 0.68$, and the bottom row the LEGA-C galaxies with $0.68 < z \leq 0.76$. The colour scale of the left column represents metallicity and the centre column shows the smoothed metallicity using the LOESS algorithm. The best-fits are shown in the left column (black solid line) with the fitted 1σ intrinsic scatter (black dotted lines). The median uncertainty on the mass, size and [Z/H] are shown by the example point in the bottom right corners of the left and right columns. In the centre column, the dashed lines show constant M_*/R_e and the dotted lines show constant surface density $\Sigma \propto M_*/R_e^2$. The right column shows the dependence of the residuals (defined as the perpendicular distance between the model minus the data) from the best-fit mass–size relation with metallicity. The black line in the right column is the best-fit relation to the residuals, with the slope written at the top of each panel. The crosses show the median value in independent bins with 3 or more galaxies. This Figure suggests that metallicity varies with M_*/R_e (dashed lines in the middle column) in all three redshift bins.

absolute age of stellar population templates is not well constrained (e.g. McDermid et al. 2015; Scott et al. 2017), and therefore we focus instead on the *relative* difference between age measurements and templates. Using the full set of templates also provides a key way to determine the reliability of our age measurements. 26 (5%) of LEGA-C age measurements are older than 8 Gyr, indicating that for 95% of the data the ages are constrained to be younger than the age of the Universe by the data alone, despite allowing for older templates. Additionally, these 26 galaxies have larger age uncertainties than the rest of the sample (mean $\sigma_{\log \mathrm{Age}} = 0.09$ dex for $\log \mathrm{Age} \geq 8$ Gyr, compared to mean $\sigma_{\log \mathrm{Age}} = 0.06$ dex for $\log \mathrm{Age} < 8$ Gyr), therefore these 26 too-old galaxies are already down-weighted in the analysis.

3.2 Linear and Planar fits

All linear fits are done using a Bayesian approach as outlined by Hogg et al. (2010) for N points with Gaussian uncertainties on x and y ($\sigma_{x,n}$, $\sigma_{y,n}$), and intrinsic variance in the y-direction (λ^2). Therefore the log-likelihood $\log p$ for slope m and intercept b is:

$$\log p = -0.5 \sum_{n=1}^{N} \left(\frac{\Delta_n^2}{\Sigma_n^2} + \log \Sigma_n^2 \right) \quad (5)$$

Where

$$\Delta_n = y_n - m x_n - b \quad (6)$$

$$\Sigma_n = (-m, 1) \cdot \begin{pmatrix} \sigma_{x,n}^2 & 0 \\ 0 & \sigma_{y,n}^2 \end{pmatrix} \cdot (-m, 1)^T + \lambda^2 \quad (7)$$

The posterior function takes uniform priors on the angle of the line and the intercept, and a Jeffreys (1946) prior on the intrinsic scatter in the y-direction ($P(\sigma) \propto 1/\sigma$).

We first find the mode of the posterior function using the differential evolution numerical method (Storn & Price 1997). This is followed by Markov Chain Monte Carlo integration of the posterior distribution to estimate the uncertainties on the model parameters, using the Python package EMCEE (Foreman-Mackey et al. 2013), which implements the affine-invariant ensemble sampler of Goodman & Weare (2010). A similar Bayesian approach is used for the plane fits in Section 4.1, with uniform priors on the slopes and intercepts and a Jeffreys (1946) prior on the intrinsic scatter in the z-direction

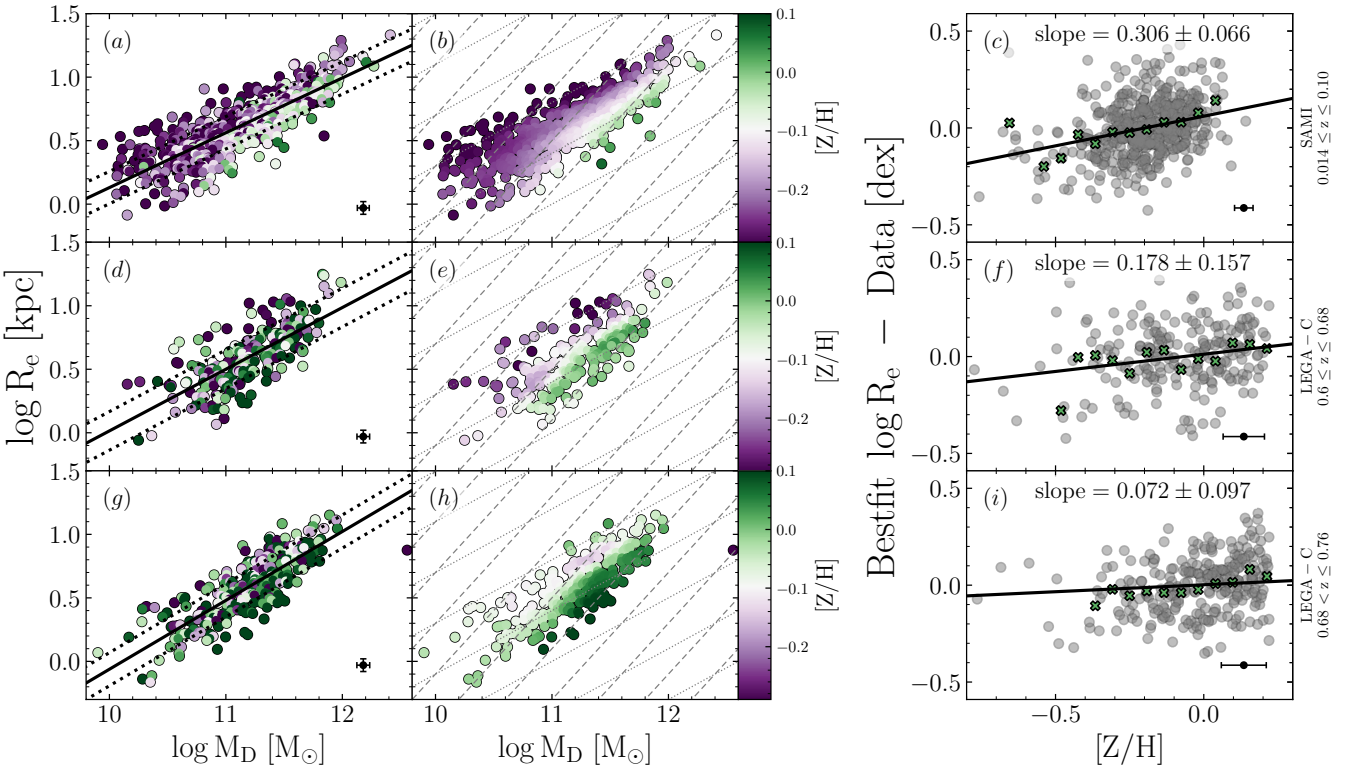


Figure 6. Stellar metallicity [Z/H] of quiescent galaxies in the dynamical mass–size plane for three redshift bins. The top row shows the SAMI galaxies $0.014 \leq z \leq 0.10$, middle row the LEGA-C galaxies with $0.60 \leq z \leq 0.68$, and the bottom row the LEGA-C galaxies with $0.68 < z \leq 0.76$. The colour scale of the left column represents metallicity and the centre column shows the smoothed metallicity using the LOESS algorithm. The best-fits are shown in the left column (black solid line) with the fitted 1σ intrinsic scatter (black dotted lines). The median uncertainty on the mass, size and [Z/H] are shown by the example point in the bottom right corner of the left and right columns. In the centre column, the dashed lines show constant M_D/R_e and the dotted lines show constant surface density $\Sigma \propto M_D/R_e^2$. The right column shows the dependence of the residuals (defined as the perpendicular distance between the model minus the data) from the best-fit mass–size relation with metallicity. The black line in the right column is the best-fit relation to the residuals, with the slope written at the top of each panel. The crosses show the median value in independent bins with 3 or more galaxies. This Figure suggests that metallicity varies with M_D/R_e (dashed lines in the middle column) in all three redshift bins.

Table 1. The Spearman correlation coefficient (ρ) and 1σ uncertainty for correlations between stellar population parameter ([Z/H] or Age) and structural parameter M, M/R_e and M/R_e^2 for both the stellar mass (M_*) and a dynamical mass estimate ($M_D \propto \sigma^2 R_e$). For each set of relations ([Z/H] or Age, M_* or M_D) we highlight in bold the structural parameter (M, M/R_e, M/R_e^2) with the highest Spearman correlation coefficient (if $\rho > 0.25$ and the difference to the next highest value is greater than $1\sigma_\rho$).

Parameter	Sample	M_*	M_*/R_e	M_*/R_e^2	M_D	M_D/R_e	M_D/R_e^2
[Z/H]	$0.014 \leq z_{SAMI} \leq 0.10$	0.55 ± 0.01	**0.66 ± 0.02**	0.36 ± 0.02	0.43 ± 0.01	**0.55 ± 0.01**	0.42 ± 0.02
[Z/H]	$0.60 \leq z_{LEGA-C} \leq 0.68$	0.26 ± 0.03	**0.37 ± 0.04**	0.23 ± 0.03	0.16 ± 0.03	**0.27 ± 0.03**	0.21 ± 0.04
[Z/H]	$0.68 < z_{LEGA-C} \leq 0.76$	0.27 ± 0.03	**0.46 ± 0.03**	0.29 ± 0.04	0.11 ± 0.03	0.30 ± 0.04	0.26 ± 0.04
Age	$0.014 \leq z_{SAMI} \leq 0.10$	0.08 ± 0.02	0.15 ± 0.02	0.13 ± 0.02	0.21 ± 0.01	0.34 ± 0.02	**0.40 ± 0.02**
Age	$0.60 \leq z_{LEGA-C} \leq 0.68$	0.12 ± 0.03	0.09 ± 0.04	0.01 ± 0.04	0.24 ± 0.03	**0.30 ± 0.03**	0.18 ± 0.04
Age	$0.68 < z_{LEGA-C} \leq 0.76$	0.11 ± 0.03	-0.07 ± 0.04	-0.11 ± 0.04	0.24 ± 0.03	0.26 ± 0.04	0.05 ± 0.04

(i.e. in metallicity). The 2 dimensional likelihood (equation 5) can be generalised to 3 dimensions with slopes m_1, m_2:

$$\Delta_n = z_n - m_1 y_n - m_2 x_n - b \tag{8}$$

$$\Sigma_n = (-m_1, -m_2, 1) \cdot \begin{pmatrix} \sigma_{x,n}^2 & 0 & 0 \\ 0 & \sigma_{y,n}^2 & 0 \\ 0 & 0 & \sigma_{z,n}^2 \end{pmatrix} \cdot (-m_1, m_2, 1)^T + \lambda^2 \tag{9}$$

For illustrative purposes we emphasise the presence/absence of residual trends by smoothing the colour distributions using the LOESS locally weighted regression algorithm (Cleveland & Devlin 1988; Cappellari et al. 2013a) with a fraction of 0.4 points used in the local approximation. However all fits are done on the unsmoothed data. The LOESS algorithm takes into account the uncertainty on the stellar population parameter (age or metallicity), therefore highly uncertain points may have a significantly different value in the LOESS smoothed colour map compared to the unsmoothed data. We note that these smoothed colour scales are useful to highlight broad age and metallicity variations in the data, but should not be interpreted as reliable for individual datapoints.

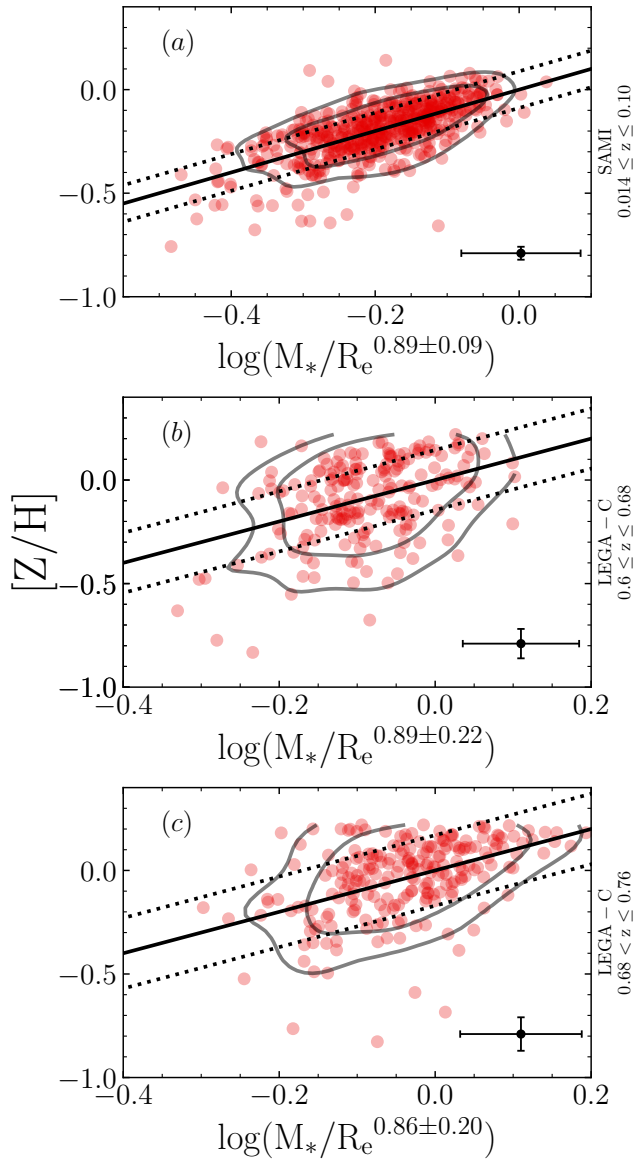


Figure 7. Stellar metallicity [Z/H] versus the best-fit linear combination of M_* and R_e for the three redshift bins. The top panel (a) shows the SAMI galaxies $0.014 \leq z \leq 0.10$, the middle panel (b) shows the LEGA-C galaxies with $0.60 \leq z \leq 0.68$, and the bottom panel (c) the LEGA-C galaxies with $0.68 < z \leq 0.76$. The best-fits are shown by the black solid line with the fitted 1σ intrinsic scatter (black dotted lines). The median uncertainty on the M_*, R_e and [Z/H] are shown by the example point in the bottom right corner of each panel. The best-fit ratio of coefficients between $\log M_*$ and $\log R_e$ is statistically consistent within $\sim 2\sigma$ across all three redshift bins and with a ratio of -1.

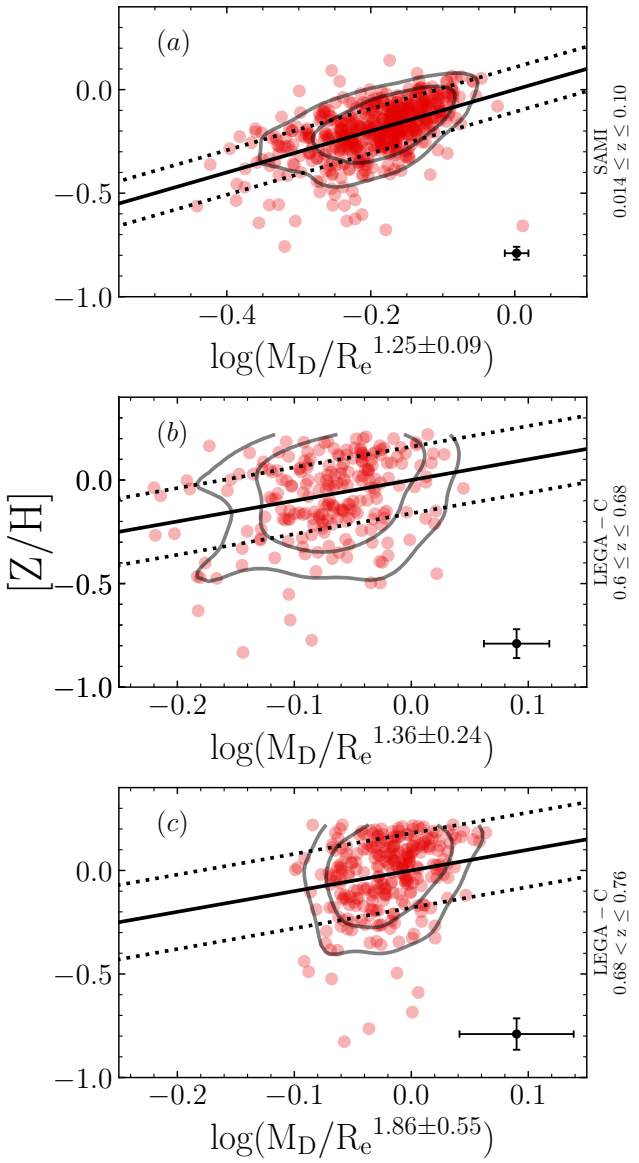


Figure 8. Stellar metallicity [Z/H] versus the best-fit linear combination of M_D and R_e for the three redshift bins. The top panel (a) shows the SAMI galaxies $0.014 \leq z \leq 0.10$, the middle panel (b) shows the LEGA-C galaxies with $0.60 \leq z \leq 0.68$, and the bottom panel (c) the LEGA-C galaxies with $0.68 < z \leq 0.76$. The best-fits are shown by the black solid line with the fitted 1σ intrinsic scatter (black dotted lines). The median uncertainty on the M_D, R_e and [Z/H] are shown by the example point in the bottom right corner of each panel. The best-fit ratio of coefficients between $\log M_D$ and $\log R_e$ is statistically consistent within $\sim 3\sigma$ across all three redshift bins and with a ratio of -1.

3.3 Non-Parametric Measure of Correlation

In Table 1 we present the Spearman rank-order correlation coefficient along with its 1σ uncertainty for the relations between stellar population parameters age and [Z/H], and the structural parameters of mass, gravitational potential, and surface-density using both M_* and M_D. We estimate the uncertainty on the Spearman coefficients by generating 1000 different datasets consistent with our original measurements. Specifically, each datapoint is sampled 1000 times from a gaussian distribution centered on the datapoint's "true" value and with a width equal to the uncertainty on that datapoint. For all relations the distribution of Spearman coefficients is consistent with Gaussian. We therefore use the standard deviation of the distribution as the uncertainty on the coefficient.

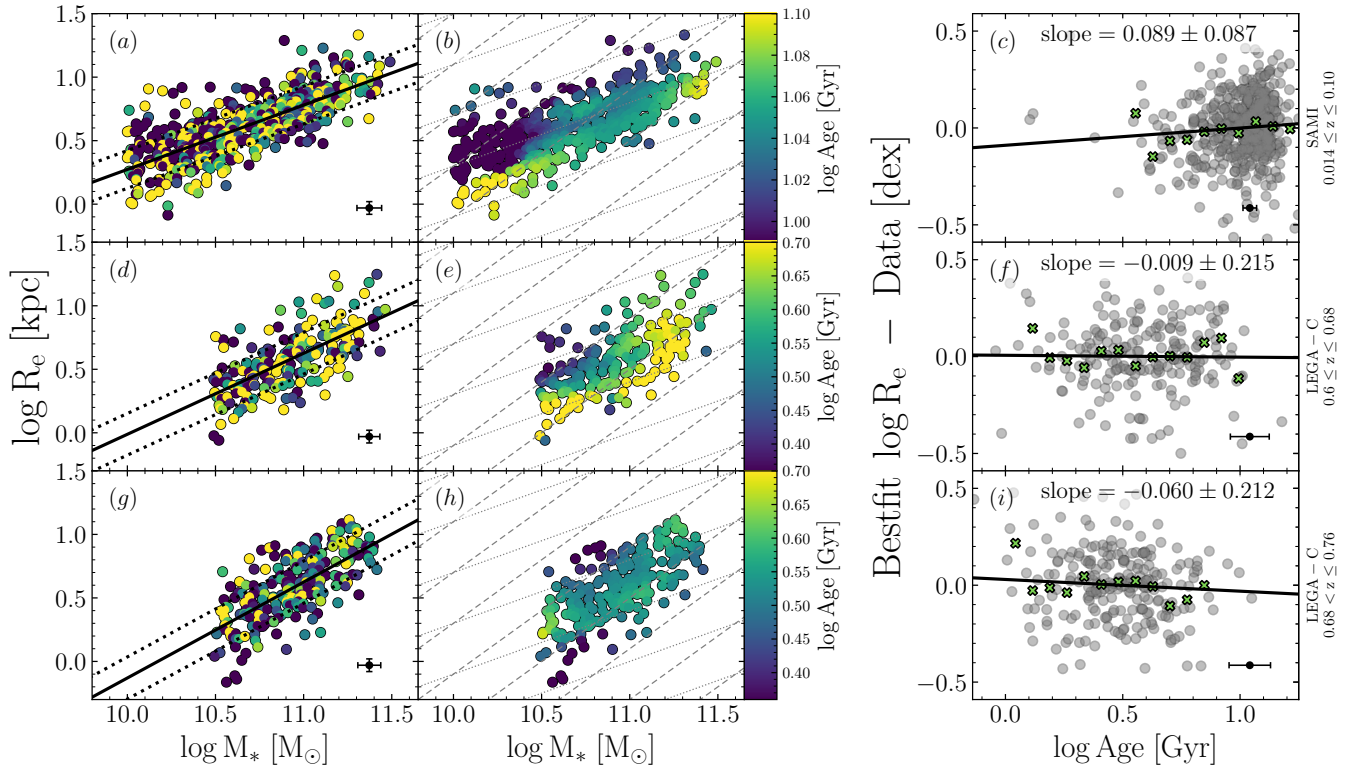


Figure 9. Stellar age in the stellar mass–size plane for quiescent galaxies in the three redshift bins. The top row shows the SAMI data with $0.014 \leq z \leq 0.10$, middle row the LEGA-C data with $0.60 \leq z \leq 0.68$, and the bottom row the LEGA-C data with $0.68 < z \leq 0.76$. The colour scale of the left column represents the stellar age, and the centre column shows the smoothed age using the LOESS algorithm. Note that the top row has a different colour scale range then the middle and bottom rows. The best-fits are shown in the left column (black solid line) with the fitted 1σ intrinsic scatter (black dotted lines). The median uncertainty on the mass, size and age are shown by the example point in the bottom right corner of the left and right columns. In the centre column the dashed lines show constant M_*/R_e and the dotted lines show constant surface mass density $\Sigma \propto M_*/R_e^2$. The right column shows the dependence of the residuals (defined as the perpendicular distance between the model minus the data) from the best-fit mass–size relation with age. The black line in the right column is the best-fit relation to the residuals, with the slope written at the top of each panel. The crosses show the median value in independent bins with 3 or more galaxies. This Figure illustrates that variations in age in the mass–size plane change with redshift.

4 RESULTS

4.1 Metallicity [Z/H]

We start by showing how luminosity-weighted [Z/H] varies in the mass–size plane using both the stellar mass M_* (Figure 5) and the dynamical mass proxy M_D (Figure 6). In all three redshift bins (rows) of Figures 5 and 6 we see significant dependence of metallicity on both mass and size. The LOESS-smoothed distributions (middle column) highlight that [Z/H] varies essentially along lines of constant M/R_e (dashed lines).

The right columns of Figures 5 and 6 quantify this variation by showing how the residuals from the best-fit mass–size relation trend with [Z/H], where the residuals are the perpendicular distance between the model minus the data. The low-redshift SAMI sample shows the strongest trend between the mass–size residuals and [Z/H], with panel c in Figures 5 and 6 both having 3σ positive trends (i.e. smaller galaxies at fixed mass are more metal rich). The LEGA-C samples also show positive trends between the residuals and [Z/H], however with decreased statistical significance due to the smaller sample size compared to SAMI.

Table 1 further emphasises the dependence of [Z/H] on M/R_e. It shows that, for both M_* and M_D, the structural parameter leading to the highest Spearman correlation coefficient is M/R_e. For stellar mass, M_*/R_e is the highest coefficient by at least $2\sigma_\rho$ for all three redshift samples. Dynamical mass shows a similar result with [Z/H]–M_D/R_e being highest with over $3\sigma_\rho$ significance for the SAMI sample, although for the LEGA-C samples the [Z/H]–M_D/R_e coefficient is less than $2\sigma_\rho$ larger than [Z/H]–M_D/R_e^2. The [Z/H]–M_D/R_e coefficients are, however, all 2-3σ_ρ larger than [Z/H]–M_D, indicating that at fixed mass [Z/H] has a significant dependence on R_e in all three redshift bins.

We further quantify the dependence of [Z/H] on both mass and size in Figures 7 and 8, which show [Z/H] fit as a linear combination of $\log M$ and $\log R_e$, [Z/H]= $a \log M + b \log R_e + c$. In Figure 7 the ratio of the coefficients of $\log M_*$ and $\log R_e$ in the best-fit relations are $a/b = -0.89 \pm 0.09, -0.89 \pm 0.22, -0.86 \pm 0.20$ for $z \in [0.014, 0.10]$, $z \in [0.60, 0.68]$, and $z \in [0.68, 0.76]$ respectively. All three ratios are within 1–2σ uncertainty of -1, the ratio representing the gravitational potential ($\Phi \propto M_*/R_e$). Furthermore these ratios are significantly different from 0 (the ratio representing scaling solely with M_*) and 2 (scaling with surface density $\Sigma \propto M_*/R_e^2$).

We find a similar result in Figure 8 using the dynamical mass proxy M_D, however we note a slight difference in the optimal coefficient ratio when using M_* and M_D; the planar fits with M_* have ratios slightly above -1 (-0.86 to -0.89), while the fits with M_D all have ratios slightly below -1 (-1.25 ± 0.09, -1.36 ± 0.24, and $-1.86 \pm$

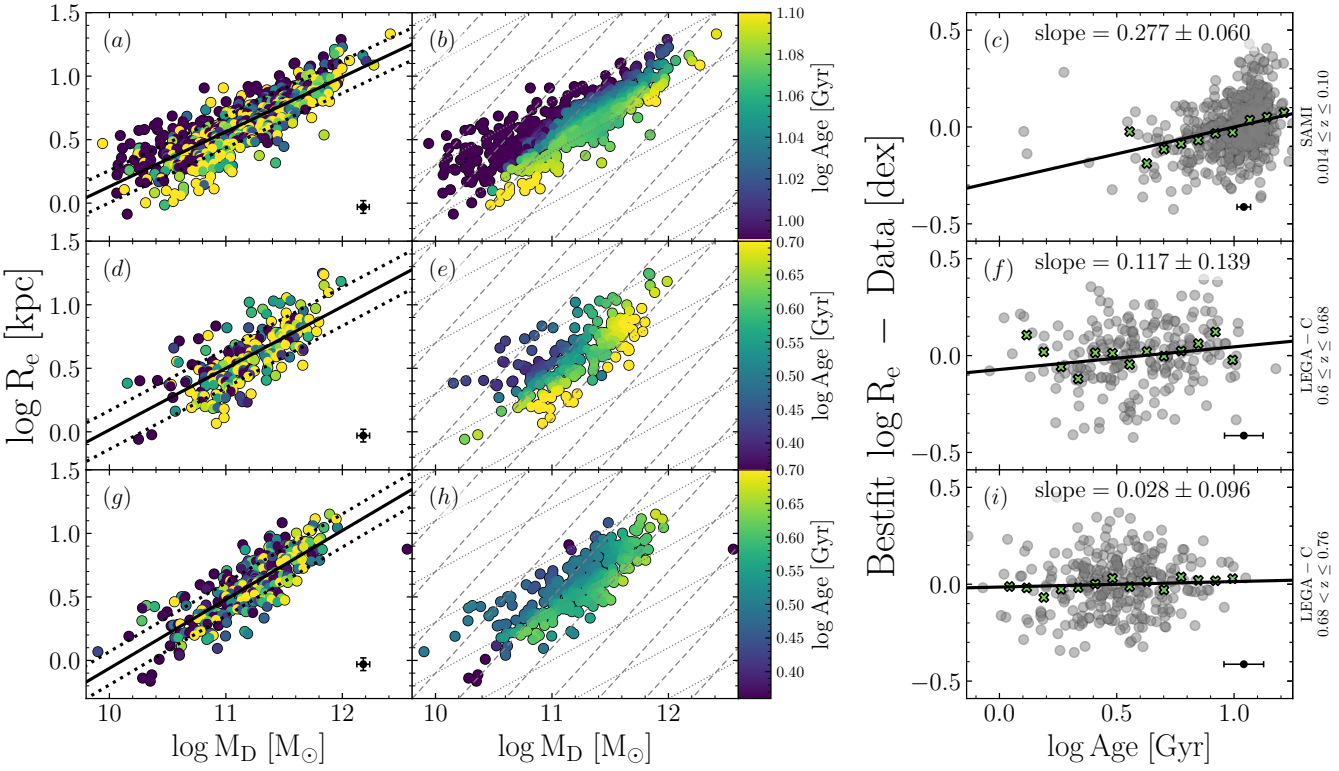


Figure 10. Stellar age in the dynamical mass–size plane for quiescent galaxies in the three redshift bins. The top row shows the SAMI data with $0.014 \leq z \leq 0.10$, middle row the LEGA-C data with $0.60 \leq z \leq 0.68$, and the bottom row the LEGA-C data with $0.68 < z \leq 0.76$. The colour scale of the left column represents the stellar age, and the centre column shows the smoothed age using the LOESS algorithm. Note that the top row has a different colour scale range then the middle and bottom rows. The best-fits are shown in the left column (black solid line) with the fitted 1σ intrinsic scatter (black dotted lines). The median uncertainty on the mass, size and age are shown by the example point in the bottom right corner of the left and right columns. In the centre column the dashed lines show constant M_D/R_e and the dotted lines show constant surface mass density $\Sigma \propto M_D/R_e^2$. The right column shows the dependence of the residuals (defined as the perpendicular distance between the model minus the data) from the best-fit mass–size relation with age. The black line in the right column is the best-fit relation to the residuals, with the slope written at the top of each panel. The crosses show the median value in independent bins with 3 or more galaxies. This Figure illustrates that variations in age in the mass–size plane change with redshift.

0.55 for $z \in [0.014, 0.10]$, $z \in [0.60, 0.68]$, and $z \in [0.68, 0.76]$ respectively). Although, similarly to Figure 7, all three ratios with M_D are within 1–3σ of −1 representing the gravitational potential. For the highest redshift bin the ratio -1.86 ± 0.55 is closer to -2, although it is still consistent within 2σ to -1. Additionally, the Spearman coefficient in the highest redshift bin is slightly higher for [Z/H]–M_D/R_e ($\rho = 0.30 \pm 0.04$) than for M_D/R_e^2 ($\rho = 0.26 \pm 0.04$).

4.2 Age

We show how luminosity-weighted age varies in the mass–size plane using both the stellar mass M_* (Figure 9) and the dynamical mass proxy M_D (Figure 10). Unlike [Z/H] which shows clear results using either M_* or M_D, the age results are clearer when using M_D compared to M_*. We therefore focus on these the results with M_D (Figure 10), and note that the results with M_* are weaker but qualitatively consistent. Overall our results show that stellar age scales with mass and size differently across redshift. For a clear visual representation of the results, we can compare the smoothed colour scale in the middle column from the lowest to the highest redshift bin (middle column, top to bottom row of Figure 10). In the lowest redshift bin there is a significant variation in age perpendicular to the best-fit mass–size relation (panels b), approximately along lines of constant surface density (dotted lines). This age trend is further highlighted by the right column (panels c) which shows the relation between age and the residuals (orthogonal distance between model − data) from the mass–size best-fit, which shows a positive trend (i.e. smaller galaxies at fixed mass are older). Additionally, Table 1 shows that the highest Spearman coefficient for the SAMI age relations with M_D is M_D/R_e^2. Figure 9b shows that age also varies perpendicular to the best-fit stellar mass–size plane at low redshift.

Unlike for the SAMI galaxies, neither LEGA-C redshift bins show a statistically significant trend with the mass–size plane residuals; the slopes in panels (f) and (i) in Figures 9 and 10 are all within 1σ of zero. From Table 1 the only LEGA-C age relation with a Spearman coefficient statistically different (at least $1\sigma_\rho$) from the next highest value is Age–M_D/R_e for $0.60 \leq z \leq 0.68$. For the highest redshift bin, $0.68 < z \leq 0.76$, the Spearman coefficient for age–M_D/R_e ($\rho = 0.26 \pm 0.04$) and age–M_D ($\rho = 0.24 \pm 0.03$) are consistent within the uncertainties. Therefore, the age goes from trending with surface density (M/R_e^2) at low redshift, to a mild trend with M/R_e in the intermediate redshift bin, to a weak trend with M or M/R_e in the highest redshift bin. The change in the correlation between age and Σ with redshift suggests the relation observed at $z \sim 0$ is built up over time and that at least one of the processes driving the evolution of mass, size and/or star formation history has a redshift dependence.

Similarly to Figures 7 and 8 for [Z/H], we performed planar fits to age as a linear combination of $\log M$ and $\log R_e$. Unlike [Z/H] however, for the LEGA-C age relations, we are unable to disentangle the weak trends between age–M and age–R_e from the strong M–R_e trend itself. As a result, in a planar fit to $\log \mathrm{Age} = a \log M + b \log R_e + c$, $\log M$ and $\log R_e$ are not independent variables. Statistically this is a multicollinearity problem, and the result is that the posterior distributions of the planar fits indicate a wide range of parameter values are plausible, because the fit becomes $\log \mathrm{Age} = (a + b) \log M + c$ and the coefficients a and b are unconstrained. Therefore we do not include these fits. We note, however, that a similar analysis for a larger subset of SAMI galaxies (B18) confirms that, at $z \sim 0$, the most precise predictor of log Age is surface mass density (whether photometric or spectroscopic).

We note in particular that in the $z \sim 0$ mass–size plane age trends along lines of constant $\Sigma \propto M/R^2$ (i.e. lines with slope = 0.5), which is remarkably similar to the slope of the quiescent population itself in the mass–size plane. This result is evident from the unsmoothed data (panel a), but clearest in the LOESS-smoothed data in panel b of Figure 10 which shows that the LOESS-smoothed age varies perpendicularly to the mass–size relation. In Section 5.2.1 we investigate how the $z \sim 0$ age–Σ relation relates to the slope of the quiescent population in the mass–size plane and show how it results from the build-up of the quiescent population over time.

5 DISCUSSION

Our aim was to investigate how scaling relations between galaxy structure and global stellar metallicity and age change across ~6 Gyr, to understand the redshift dependence in stellar population evolution. We aimed to test two hypotheses:

(i) The [Z/H]–M/R_e relation is consistent with the gravitational potential regulating the retention of stellar and supernova ejecta via its relation to the escape velocity; if this is true, there should be a relation at every redshift.

(ii) The $z \sim 0$ age–Σ relation is built up over time due to galaxies forming and evolving more compactly (diffusely) at higher (lower) redshifts; in this case, the age–Σ relation should be less prominent at intermediate redshifts than at $z \sim 0$.

Our results support both these hypotheses: (i) The metallicity of intermediate-redshift quiescent galaxies, like that of low-redshift quiescent (B18) and star-forming galaxies (B20), is strongly correlated with M/R_e (Section 4.1); we discuss this further in Section 5.1. (ii) At intermediate redshifts, there is no statistically significant correlation between global stellar age and surface mass density (Section 4.2). We show how the $z \sim 0$ age–Σ is consistent with the redshift-evolution of the mass–size plane in Section 5.2.1 and further discuss this hypothesis in Section 5.2.

5.1 The consistency of the [Z/H]–Φ relation across 6 Gyr

We find that from low to intermediate redshift ($z \leq 0.76$) the stellar metallicity of quiescent galaxies correlates more tightly with M/R_e than with other combinations of mass and size. This result is in agreement with the low-redshift results of B18 and B20 for the stellar metallicity of quiescent and star-forming galaxies respectively and D'Eugenio et al. (2018) for the gas-phase metallicity of star-forming galaxies. Our results also agree with Díaz-García et al. (2019), who showed that (at fixed mass) smaller quiescent galaxies are more metal-rich since $z \sim 1$. We note that, for non-zero uncertainty on R_e, M_*/R_e^x must have a higher observational uncertainty than M_* alone (for $x \neq 0$). Therefore, our result that the observed [Z/H]–$M_*/R^{\sim 1}$ relation is tighter than the relation with M_* alone means the relation with $M_*/R^{\sim 1}$ must be *intrinsically* tighter.

These studies (B18, D'Eugenio et al. 2018, B20) built on earlier works (e.g. Worthey et al. 1992; Trager et al. 2000) that proposed the global stellar and gas-phase metallicity of a galaxy is regulated by the gravitational potential (Φ), as the depth of the potential well determines the escape velocity required for metal-rich gas to be expelled from the system by supernova, active galactic nuclei (AGN) and/or stellar winds and thus avoid being recycled into later stellar generations. Our finding that the relation also exists at $0.60 \leq z \leq 0.76$ supports this hypothesis.

It is interesting to note that the ratio of coefficients of the best-fit planes for the three samples are all consistent within 1σ (for either M_* or M_D). If we simplify the complex process of metal production and outflows to a closed box model and assume the global stellar metallicity results from a balance between metal production determined by the stellar mass and metal retention determined by the gravitational potential and the strength and frequency of gas outflows, our results are consistent with there being no significant change in the balance of these processes from $0.014 \leq z \leq 0.76$. While we are unable to quantitatively test this hypothesis due to differences in the sample selection between the two surveys, future works focusing on the slope and scatter of the [Z/H]–Φ relation across redshift may shed light on this topic, and help place constraints on the strength and efficiency of feedback process in heating and expelling interstellar gas.

5.2 The build-up of the age–Σ relation over 6 Gyr

Unlike the metallicity results, we find a significant difference between the age distribution in the mass–size plane at intermediate redshift compared to low redshift. B18 and B20 found that the global age of both low-redshift early-type and star-forming galaxies tightly correlates with the surface density ($\Sigma \propto M/R_e^2$), whereas we find no significant correlation with Σ in either LEGA-C redshift sample. Comparing the results from the highest to lowest redshift bin, age changes from varying weakly with M and/or M/R_e ($0.68 < z \leq 0.76$), to weakly correlating with M/R_e ($0.6 \leq z \leq 0.68$), to a significant variation with M/R_e^2, approximately *perpendicular* to the mass–size relation ($0.014 \leq z \leq 0.10$). This suggests that, unlike the [Z/H]–Φ relation, the $z \sim 0$ age–Σ does not reflect a causal relation, but is instead built up over time due to the fact that both age and Σ depend on the conditions of the Universe when a galaxy becomes quiescent. This hypothesis is supported by a number of studies linking age, Σ, and formation epoch. In particular, Kauffmann et al. (2003, 2006) and Franx et al. (2008) showed that galaxy star formation histories are strongly correlated with surface mass density. This correlation between star formation history and surface density was further refined by Díaz-García et al. (2019) and Zolotov et al. (2015), who showed that central surface density correlates strongly with formation epoch and quenching epoch respectively. We build upon these previous work to relate the change across redshift of the age dependence on mass and size to the evolution of the mass–size relation in the following Section 5.2.1, and show that we can explain the $z \sim 0$ age–Σ relation as being due to the average surface density of galaxies in both the star-forming and quiescent populations decreasing with decreasing redshift.

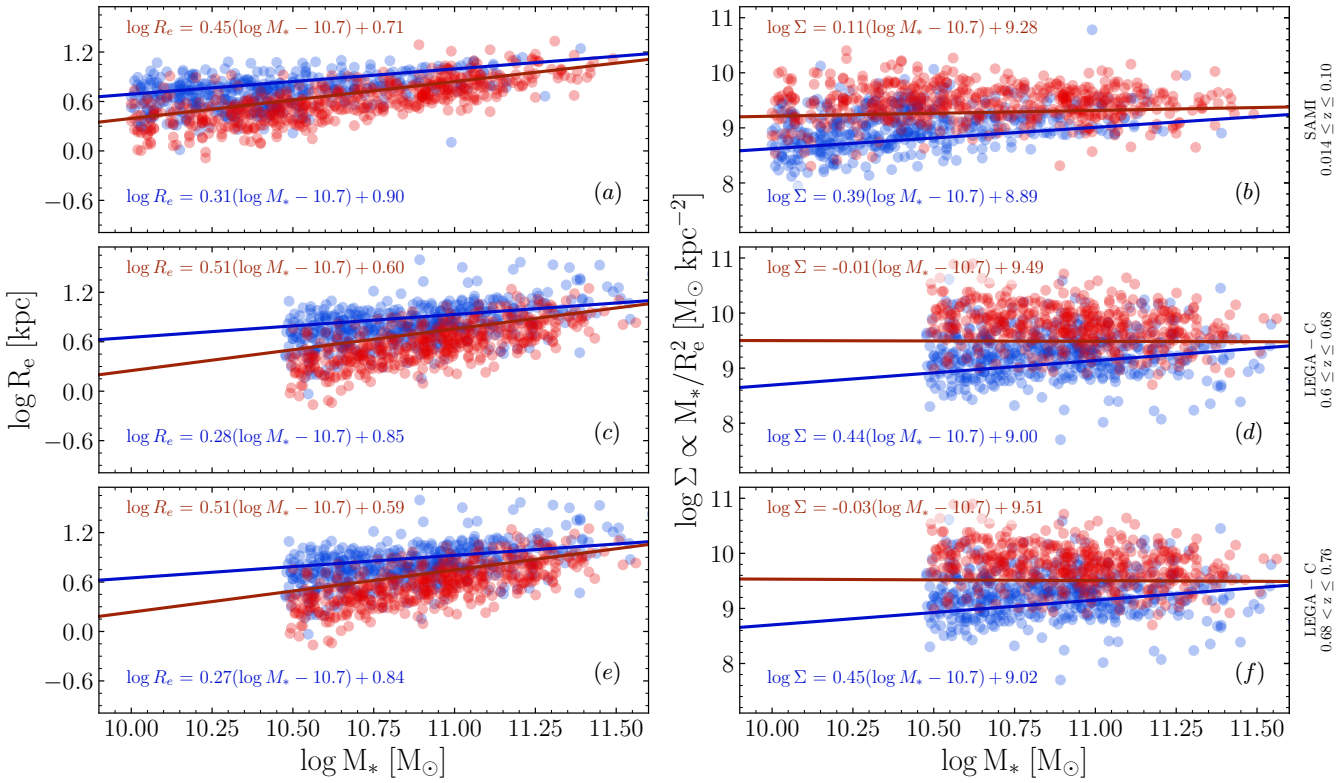


Figure 11. Mass–size (left column) and mass–surface density (right column) planes for the three redshifts bins. The top row shows the SAMI data with $0.014 \leq z \leq 0.10$, middle row the LEGA-C data with $0.60 \leq z \leq 0.68$, and the bottom row the LEGA-C data with $0.68 < z \leq 0.76$. The red points are quiescent galaxies and the blue points are star-forming galaxies. In the left columm, the solid red and blue lines are the redshift-dependent mass–size relations to the quiescent and star-forming populations based on the analysis of Mowla et al. (2019). The equations for these relations are written in each panel (in red at the top for quiescent galaxies and in blue at bottom for star-forming galaxies). In the right column, we show the same mass–size relations from Mowla et al. (2019) converted to the mass–surface density plane.

5.2.1 Age in the mass–size and mass–surface density planes

It is well established that the median size of galaxies in both the quiescent and star-forming populations evolves significantly in the mass–size plane with redshift (Ferguson et al. 2004; Trujillo et al. 2007; Buitrago et al. 2008; Williams et al. 2010). Specifically, van der Wel et al. (2014) and Mowla et al. (2019) showed that for $0 \leq z \leq 3$, the slopes of the mass–size relations for both the quiescent and star-forming populations change little with redshift, but the intercepts decrease with increasing redshift such that high-redshift populations are smaller at fixed mass.

We illustrate this result in the left column of Figure 11, which shows our quiescent and star-forming populations in the mass–size plane for each redshift bin. The solid blue and red lines are the redshift-dependent best-fit stellar mass–size relations from Mowla et al. (2019). The left column of Figure 11 shows that, while our quiescent galaxy mass estimates are systematically slightly below the Mowla et al. (2019) relations, our samples are in overall good agreement.

Of crucial importance are the slopes of mass–size relations for the quiescent populations. In all three redshift bins the mass–size relation for the quiescent population is approximately $\log R_e \approx 0.5 \log M_*$ (specifically, 0.45, 0.51 and 0.51 for $z \in [0.014, 0.10]$, $z \in [0.60, 0.68]$ and $z \in [0.68, 0.76]$ respectively). This slope of ∼0.5 in the mass–size plane means that, at fixed redshift, the quiescent population has an approximately constant surface–mass density regardless of stellar mass. For some redshift-dependent constant $k_1(z)$,

$$\log R_e = 0.5 \log M_* + k_1(z) \quad (10)$$

$$\log \Sigma = \log M_* - 2 \log R_e = -2k_1(z) \quad (11)$$

which implies that surface density does not change with stellar mass:

$$\frac{\delta \log \Sigma}{\delta \log M_*} = 0 \quad (12)$$

Indeed, in the right column of Figure 11 we show our samples in the stellar mass–surface density plane. The red and blue lines are the mass–size relations from Mowla et al. (2019) converted to be in terms of mass and surface density. As expected given the mass–size relations in the left column, the slopes of the quiescent populations are all close to zero (0.11, -0.01, and -0.01 for $z \in [0.014, 0.10]$, $z \in [0.60, 0.68]$ and $z \in [0.68, 0.76]$). Furthermore, as expected, the intercepts in the mass–surface density plane increase with increasing redshift, such that the LEGA-C quiescent galaxies are more compact (higher Σ) than the lower redshift SAMI quiescent galaxies.

The individual evolutionary tracks of star-forming galaxies are expected to closely align with the star-forming population in the mass–size plane, a result supported by both observations and simulations (Lilly et al. 1998; Ravindranath et al. 2004; Trujillo et al. 2006; van Dokkum et al. 2015). Therefore the slope of ∼0.3 for the star-forming sequence in the mass–size plane in all three redshift bins means that as galaxies build up their mass via in-situ star formation,

they also increase their surface density. For some redshift-dependent constant $k_2(z)$,

$$\log R_e = 0.3 \log M_* + k_2(z) \quad (13)$$

$$\log \Sigma = \log M_* - 2 \log R_e = 0.4 \log M_* - 2k_2(z) \quad (14)$$

which implies surface density increases with increasing stellar mass:

$$\frac{\delta \log \Sigma}{\delta \log M_*} = 0.4 \quad (15)$$

Combining these two key results suggests that star-forming galaxies build their stellar mass, and at the same time increase their stellar surface density until they reach a redshift-dependent threshold surface density at which they quench. As this threshold surface density decreases with decreasing redshift, the quiescent population is built up to include galaxies that have quenched at a range of redshifts and, consequently, with a range of surface densities. In the $z \sim 0$ quiescent population, therefore, a galaxy's surface density reflects the redshift at which it quenched (luminosity-weighted age is closely tied to how long ago the galaxy quenched).

This connection between quenching and galaxy structure, in particular surface density, is in agreement with previous work. Franx et al. (2008) found a redshift-dependent threshold surface density above which galaxies have low sSFR (are quiescent) and below which the sSFR are high with little variation (are star-forming). Franx et al. (2008) also found that the surface density threshold increases with increasing redshift. Similarly, van der Wel et al. (2009) found that stellar velocity dispersion also shows a redshift-dependent threshold separating quiescent and star-forming galaxies. Additionally, González Delgado et al. (2014a) found a threshold surface-mass density for low-redshift spheroidal galaxies that is nearly independent of stellar mass, in agreement with our results.

Recent work by Chen et al. (2020) provides a theoretical framework explaining the relation between surface density and quenching. Chen et al. (2020) showed that a galaxy model in which central black hole mass (and therefore strength of AGN feedback) is related to both the host galaxy's mass and size successfully explains key properties of star-forming and quenched galaxies. In the model larger star-forming galaxies at fixed mass have smaller central super-massive black holes (due to their lower central surface density). Therefore these extended galaxies evolve to higher stellar masses before the central AGN has strong enough feedback to shock-heat infalling gas from the halo, quenching star formation.

There remain two unanswered questions: (1) what leads to galaxies forming more compactly at higher redshifts? and (2) what leads to the decrease with time of the redshift-dependent threshold surface density at which star-forming galaxies quench? In relation to the first question, Franx et al. (2008) concluded that compact galaxies must have formed their stars earlier when the Universe was denser and had a higher gas fraction compared to the formation epoch of galaxies with lower surface densities. Wellons et al. (2015) used the Illustris simulations (Genel et al. 2014; Vogelsberger et al. 2014) to trace the star-formation and assembly histories of compact galaxies and found that another dominant mechanism for forming compact galaxies at high redshift are centrally-concentrated starbursts triggered by wet major mergers. Wellons et al. (2015) noted that this wet major merger mechanism is also intrinsically linked to the density and redshift evolution of the Universe; as the Universe expanded and the abundance of cold gas decreased, the likelihood of wet major mergers also decreased with decreasing redshift. While these explanations may underlie the change in the formation and evolution of galaxies across redshift (question 1), they do not explain the origin of the redshift-dependent surface density threshold at which star-forming galaxies quench (question 2). This changing threshold may be due a redshift-dependence of the complex balance between the supply and heating of inflowing gas and the feedback and outflows from star formation and AGN (e.g., Chen et al. 2020).

Clearly, this scenario of a redshift-dependent quenching surface-density requires that passive evolution does not significantly alter the inner structure of quiescent galaxies (inside $\sim 1\ R_e$); however, we note that if this assumption was incorrect, it would be even harder to explain the observed correlation between stellar population age and surface mass density.

5.2.2 *The effect of mergers*

Thus far we have only considered the evolution in the average properties of the quiescent and star-forming populations due to the addition (and loss) of new (and old) members. However individual galaxies also grow in mass and size through both minor (mass ratio $\lesssim 0.3$ e.g. Lambas et al. 2012) and major mergers (Oser et al. 2012; Bluck et al. 2012; Oogi & Habe 2013; Ownsworth et al. 2014). Indeed, the relative absence at low redshift of the very compact galaxies frequently observed at high redshift indicates individual galaxies must undergo significant mass–size evolution even after ceasing star formation (van Dokkum et al. 2010). Dry major mergers are expected to increase a galaxy's mass and size proportionally, whereas minor mergers significantly increase a galaxy's effective radius while contributing comparatively little to its stellar mass (Bezanson et al. 2009; Naab et al. 2009; Hopkins et al. 2009). Given these two relations, both major and minor mergers will increase a galaxy's mass but *decrease* its surface mass density and therefore move galaxies down and right in the mass–Σ plane. Specifically, based on results from Naab et al. (2009) and Bezanson et al. (2009):

$$\Delta \log R_{e,major} \approx \Delta \log M_* \quad (16)$$

$$\Delta \log R_{e,minor} \approx 2\Delta \log M_* \quad (17)$$

Therefore the changes in surface mass density are always negative (galaxies become more diffuse):

$$\Delta \log \Sigma_{major} \approx -\Delta \log M_* \quad (18)$$

$$\Delta \log \Sigma_{minor} \approx -3\Delta \log M_* \quad (19)$$

We can explore the implications of mergers on the build-up of the age–surface density relation by considering a hypothetical scenario in which galaxies quench at a surface density *independent* of redshift (i.e. there is no redshift evolution of the mass–size plane). If we consider only mass growth through mergers (i.e. no star-formation) and assume that older galaxies (those that formed earlier) will on average have undergone more mergers than younger galaxies, this would lead to older galaxies having on average a *lower* surface density than young galaxies at fixed mass—the opposite of the trend seen at $z \sim 0$. Therefore, while individual galaxy evolution through mergers will undoubtedly introduce scatter into the relation, it cannot be the cause of our age results; in fact, it suggests the original relation must be even stronger than observed today. In addition to increasing a galaxy's mass and size, mergers also influence global stellar population properties. In particular the old, metal rich stellar populations of massive compact galaxies are diluted with younger metal-poor stars when merging with smaller, more diffuse systems. Furthermore, mergers can also restart star-formation in quenched galaxies, lowering the mean stellar population age and metallicity. At $z < 1$ between 10–15% of quiescent galaxies are estimated to have undergone rejuvenated star formation (Thomas et al. 2010; Chauke

et al. 2019), which may account for some of the intrinsic scatter in the age–Σ correlation.

6 SUMMARY AND CONCLUSIONS

In this study we aimed to test two key hypotheses on the origins of low redshift stellar population scaling relations:

(i) The [Z/H]–M/R_e relation at $z \sim 0$ is due to the gravitational potential regulating the retention of stellar and supernova ejecta via its relation to the escape velocity. If so, there should also be a tight correlation between [Z/H] and M/R_e at intermediate ($z \sim 0.7$) redshifts.

(ii) The age–Σ relation at $z \sim 0$ is built up over time due to galaxies forming and evolving more compactly (diffusely) at higher (lower) redshifts. If true, at intermediate redshifts the age–Σ relation should be less prominent.

To achieve these goals, we used pPXF and the E-MILES library of synthetic stellar templates to measure global light-weighted stellar ages and metallicities for a representative sample of quiescent galaxies spanning 6 Gyr of cosmic history. The data consists of 524 quiescent galaxies with $0.014 \leq z \leq 0.10$ from the SAMI Galaxy Survey, and 492 quiescent galaxy split between $0.60 \leq z \leq 0.68$ and $0.68 < z \leq 0.76$ from the LEGA-C Survey. We quantified how the global stellar population parameters of age and metallicity vary in the mass–size plane between low ($0.014 \leq z \leq 0.10$) and intermediate ($0.60 \leq z \leq 0.76$) redshifts. Specifically, we investigated whether the [Z/H]–M/R_e and age–M/R_e^2 relations found at low redshift by B18 for quiescent galaxies are also present in a sample with similar masses at a lookback time of 6 Gyr. We find the [Z/H]–M/R_e relation is also present at intermediate redshifts but the age–M/R_e^2 relation is not, in agreement with both our hypotheses.

Our conclusion that the [Z/H]–M/R_e also exists at $0.60 \leq z \leq 0.76$ extends our previous results at low redshift for stars (B18; B20) and gas (D'Eugenio et al. 2018) and supports the theory that the depth of the gravitational potential well regulates the stellar and gas-phase metallicity by determining the escape velocity required for metal-rich gas to be expelled from the system and thus avoid being recycled into later stellar generations (e.g. Franx & Illingworth 1990).

To understand the change in the way age varies across the mass–size plane from low to intermediate redshift, we consider the evolution of the mass–size plane itself. Specifically, we show that the slope of ~0.5 for the quiescent population in the mass–size plane in this redshift range (Mowla et al. 2019) leads to flat slopes in the mass–surface density plane, with an intercept that decreases with decreasing redshift. This implies that star-forming galaxies reach a redshift-dependent threshold surface density at which they quench. Importantly this threshold is higher at higher redshifts, so that galaxies forming and evolving at higher redshifts reach a higher surface density before quenching compared to low-redshift star-forming galaxies. The age–surface density relation at $z \sim 0$ is therefore the result of the build-up of the low redshift quiescent and star-forming populations from galaxies that have formed, evolved, and quenched over a range of redshifts, and hence over a range of surface densities. Consequently, the age–surface density relation at $z \sim 0$ arises from the cumulative effect of the redshift-dependent processes that drive the evolution of the star-forming and quiescent populations in the mass–size plane.

Future spectroscopic surveys such as MOONRISE (Maiolino et al. 2020) will help to push this relation to higher redshift ($z \sim 1 - 2.5$) while the large sample size and mass range of the Hector survey (Bryant et al. 2020) at $z \sim 0$ will allow exploration of these relations in the low-mass regime.

7 ACKNOWLEDGEMENTS

We thank the anonymous referee for their attention to detail which helped improve the paper. TMB is supported by an Australian Government Research Training Program Scholarship. FDE and AvdW acknowledge funding through from the European Research Council (ERC) under the European Union's Horizon 2020 research and innovation program, grant agreement No. 683184. FDE also acknowledges funding through the ERC Advanced grant 695671 "QUENCH" and support by the Science and Technology Facilities Council (STFC). NS acknowledges the support of an Australian Research Council Discovery Early Career Research Award (project number DE190100375). JvdS acknowledges support of an Australian Research Council Discovery Early Career Research Award (project number DE200100461) funded by the Australian Government. P.F.W. acknowledges the support of the fellowship from the East Asian Core Observatories Association. RB gratefully acknowledges funding provided by the Robert C. Smith Fund and the Betsy R. Clark Fund of The Pittsburgh Foundation. LC is the recipient of an Australian Research Council Future Fellowship (FT180100066) funded by the Australian Government. JBH is supported by an ARC Laureate Fellowship FL140100278. The SAMI instrument was funded by Bland-Hawthorn's former Federation Fellowship FF0776384, an ARC LIEF grant LE130100198 (PI Bland-Hawthorn) and funding from the Anglo-Australian Observatory. JJB acknowledges support of an Australian Research Council Future Fellowship (FT180100231). MSO acknowledges the funding support from the Australian Research Council through a Future Fellowship (FT140100255).

This research was supported by the Australian Research Council Centre of Excellence for All Sky Astrophysics in 3 Dimensions (ASTRO 3D) through project CE170100013.

The LEGA-C Public Spectroscopy Survey observations were made with ESO Telescopes at the La Silla Paranal Observatory under program IDs 194-A.2005 and 1100.A-0949.

The SAMI Galaxy Survey is based on observations made at the Anglo-Australian Telescope. The Sydney-AAO Multi-object Integral field spectrograph (SAMI) was developed jointly by the University of Sydney and the Australian Astronomical Observatory. The SAMI input catalogue is based on data taken from the Sloan Digital Sky Survey, the GAMA Survey and the VST ATLAS Survey. The SAMI Galaxy Survey is supported by the Australian Research Council Centre of Excellence for All Sky Astrophysics in 3 Dimensions (ASTRO 3D) through project number CE170100013, the Australian Research Council Centre of Excellence for All-sky Astrophysics (CAASTRO), through project number CE110001020, and other participating institutions. The SAMI Galaxy Survey website is http://sami-survey.org/.

We acknowledge the traditional custodians of the land on which the AAT stands, the Gamilaraay people, and pay our respects to their elders past and present.

This research was conducted using the freely available Python programming language (Van Rossum & Drake Jr 1995), maintained and distributed by the Python Software Foundation, and the IPython extension (Perez & Granger 2007). Our analysis made use of the NumPy (van der Walt et al. 2011), SciPy (Virtanen et al. 2020), Astropy (Astropy Collaboration et al. 2013), matplotlib (Hunter 2007), and corner (Foreman-Mackey 2016) packages. In preliminary analyses, we also used TOPCAT (Taylor 2005) and Ned

Wright's Cosmology Calculator (Wright 2006). We make extensive use of NASA's Astrophysics Data System.

DATA AVAILABILITY

The SAMI data used in this work is publically available and hosted on the Australian Astronomical Optics' Data Central (https://datacentral.org.au/ Croom et al. 2021a). The LEGA-C data used is in the public domain via the ESO Science Archive and through the Mikulski Archive for Space Telescopes (MAST). The full reduced data is available in the third public data release. Details of the data release are hosted on the ESO website (http://archive.eso.org/cms/eso-archive-news/Third-and-final-release-of-the-Large-Early-Galaxy-Census-LEGA-C-Spectroscopic-Public-Survey-published.html van der Wel et al. 2021).

REFERENCES

Abazajian K. N., et al., 2009, ApJS, 182, 543
Abramson L. E., Gladders M. D., Dressler A., Oemler Augustus J., Poggianti B., Vulcani B., 2016, ApJ, 832, 7
Allen J. T., et al., 2015, MNRAS, 446, 1567
Almaini O., et al., 2017, MNRAS, 472, 1401
Andrews S. K., Driver S. P., Davies L. J. M., Kafle P. R., Robotham A. S. G., Wright A. H., 2017, MNRAS, 464, 1569
Astropy Collaboration et al., 2013, A&A, 558, A33
Balogh M. L., Morris S. L., Yee H. K. C., Carlberg R. G., Ellingson E., 1999, ApJ, 527, 54
Barone T. M., et al., 2018, ApJ, 856, 64
Barone T. M., D'Eugenio F., Colless M., Scott N., 2020, ApJ, 898, 62
Barro G., et al., 2013, ApJ, 765, 104
Bell E. F., de Jong R. S., 2000, MNRAS, 312, 497
Bell E. F., Barnaby D., Bower R. G., de Jong R. S., Harper D. A., Hereld M., Loewenstein R. F., Rauscher B. J., 2000, MNRAS, 312, 470
Bezanson R., van Dokkum P. G., Tal T., Marchesini D., Kriek M., Franx M., Coppi P., 2009, ApJ, 697, 1290
Bland-Hawthorn J., et al., 2011, Optics Express, 19, 2649
Bluck A. F. L., Conselice C. J., Buitrago F., Grützbauch R., Hoyos C., Mortlock A., Bauer A. E., 2012, ApJ, 747, 34
Bruzual G., Charlot S., 2003, MNRAS, 344, 1000
Bryant J. J., Bland-Hawthorn J., Fogarty L. M. R., Lawrence J. S., Croom S. M., 2014, MNRAS, 438, 869
Bryant J. J., et al., 2015, MNRAS, 447, 2857
Bryant J. J., et al., 2020, in Society of Photo-Optical Instrumentation Engineers (SPIE) Conference Series. p. 1144715, doi:10.1117/12.2560309
Buitrago F., Trujillo I., Conselice C. J., Bouwens R. J., Dickinson M., Yan H., 2008, ApJ, 687, L61
Calzetti D., Armus L., Bohlin R. C., Kinney A. L., Koornneef J., Storchi-Bergmann T., 2000, ApJ, 533, 682
Cappellari M., 2017, MNRAS, 466, 798
Cappellari M., Emsellem E., 2004, PASP, 116, 138
Cappellari M., et al., 2006, Monthly Notices of the Royal Astronomical Society, 366, 1126
Cappellari M., et al., 2013a, MNRAS, 432, 1862
Cappellari M., et al., 2013b, MNRAS, 432, 1709
Carollo C. M., et al., 2013, ApJ, 773, 112
Chabrier G., 2003, PASP, 115, 763
Charlot S., Fall S. M., 2000, ApJ, 539, 718
Chauke P., et al., 2018, ApJ, 861, 13
Chauke P., et al., 2019, ApJ, 877, 48
Chen Z., et al., 2020, ApJ, 897, 102
Choi J., Conroy C., Moustakas J., Graves G. J., Holden B. P., Brodwin M., Brown M. J. I., van Dokkum P. G., 2014, ApJ, 792, 95
Cleveland W. S., Devlin S. J., 1988, Journal of the American Statistical Association, 83, 596
Croom S. M., et al., 2012, MNRAS, 421, 872
Croom S. M., et al., 2021a, arXiv e-prints, p. arXiv:2101.12224
Croom S. M., et al., 2021b, arXiv e-prints, p. arXiv:2105.10179
D'Eugenio F., Colless M., Groves B., Bian F., Barone T. M., 2018, MNRAS, 479, 1807
D'Eugenio F., et al., 2020, MNRAS, 497, 389
Daddi E., et al., 2007, ApJ, 670, 156
Daddi E., et al., 2010, ApJ, 713, 686
Davies L. J. M., et al., 2015, MNRAS, 447, 1014
Díaz-García L. A., et al., 2019, A&A, 631, A158
Dopita M. A., Sutherland R. S., 2003, Astrophysics of the diffuse universe. Springer
Dressler A., Gunn J. E., 1983, ApJ, 270, 7
Dressler A., Smail I., Poggianti B. M., Butcher H., Couch W. J., Ellis R. S., Oemler Augustus J., 1999, ApJS, 122, 51
Driver S. P., et al., 2011, MNRAS, 413, 971
Driver S. P., et al., 2018, MNRAS, 475, 2891
Epinat B., et al., 2012, A&A, 539, A92
Fan L., Lapi A., De Zotti G., Danese L., 2008, ApJ, 689, L101
Fan L., Lapi A., Bressan A., Bernardi M., De Zotti G., Danese L., 2010, ApJ, 718, 1460
Ferguson H. C., et al., 2004, ApJ, 600, L107
Foreman-Mackey D., 2016, The Journal of Open Source Software, 1, 24
Foreman-Mackey D., Hogg D. W., Lang D., Goodman J., 2013, PASP, 125, 306
Förster Schreiber N. M., et al., 2006, ApJ, 645, 1062
Förster Schreiber N. M., et al., 2009, ApJ, 706, 1364
Franx M., Illingworth G., 1990, ApJ, 359, L41
Franx M., van Dokkum P. G., Förster Schreiber N. M., Wuyts S., Labbé I., Toft S., 2008, ApJ, 688, 770
Gallazzi A., Bell E. F., Zibetti S., Brinchmann J., Kelson D. D., 2014, The Astrophysical Journal, 788, 25
Genel S., et al., 2014, MNRAS, 445, 175
Girardi L., Bressan A., Bertelli G., Chiosi C., 2000, A&AS, 141, 371
González Delgado R. M., et al., 2014a, A&A, 562, A47
González Delgado R. M., et al., 2014b, ApJ, 791, L16
González Delgado R. M., et al., 2015, A&A, 581, A103
Goodman J., Weare J., 2010, Communications in Applied Mathematics and Computational Science, Vol.~5, No.~1, p.~65-80, 2010, 5, 65
Green A. W., et al., 2018, MNRAS, 475, 716
Gupta A., Tran K.-V., Pillepich A., Yuan T., Harshan A., Rodriguez-Gomez V., Genel S., 2021, ApJ, 907, 95
Hill D. T., et al., 2011, MNRAS, 412, 765
Hogg D. W., Bovy J., Lang D., 2010, arXiv e-prints, p. arXiv:1008.4686
Hopkins P. F., Bundy K., Murray N., Quataert E., Lauer T. R., Ma C.-P., 2009, MNRAS, 398, 898
Hunter J. D., 2007, Computing In Science & Engineering, 9, 90
Jeffreys H., 1946, Proc. R. Soc. Lond., 186, 453–461
Kassin S. A., et al., 2012, ApJ, 758, 106
Kauffmann G., et al., 2003, MNRAS, 341, 54
Kauffmann G., Heckman T. M., De Lucia G., Brinchmann J., Charlot S., Tremonti C., White S. D. M., Brinkmann J., 2006, MNRAS, 367, 1394
Kelvin L. S., et al., 2012, MNRAS, 421, 1007
Kriek M., van Dokkum P. G., Franx M., Illingworth G. D., Magee D. K., 2009, ApJ, 705, L71
Labbé I., et al., 2005, ApJ, 624, L81
Lambas D. G., Alonso S., Mesa V., O'Mill A. L., 2012, A&A, 539, A45
Law D. R., Steidel C. C., Erb D. K., Larkin J. E., Pettini M., Shapley A. E., Wright S. A., 2007, ApJ, 669, 929
Law D. R., Steidel C. C., Erb D. K., Larkin J. E., Pettini M., Shapley A. E., Wright S. A., 2009, ApJ, 697, 2057
Le Fèvre O., et al., 2003, in Iye M., Moorwood A. F. M., eds, Society of Photo-Optical Instrumentation Engineers (SPIE) Conference Series Vol. 4841, Instrument Design and Performance for Optical/Infrared Ground-based Telescopes. pp 1670–1681, doi:10.1117/12.460959
Leslie S. K., et al., 2020, ApJ, 899, 58

Li H., et al., 2018, MNRAS, 476, 1765
Lilly S. J., Le Fevre O., Hammer F., Crampton D., 1996, ApJ, 460, L1
Lilly S., et al., 1998, ApJ, 500, 75
Madau P., Dickinson M., 2014, ARA&A, 52, 415
Madau P., Pozzetti L., Dickinson M., 1998, ApJ, 498, 106
Maiolino R., et al., 2020, The Messenger, 180, 24
McDermid R. M., et al., 2015, MNRAS, 448, 3484
Medling A. M., et al., 2018, MNRAS, 475, 5194
Moles M., et al., 2008, AJ, 136, 1325
Møller P., Christensen L., 2020, MNRAS, 492, 4805
Morokuma-Matsui K., Baba J., 2015, MNRAS, 454, 3792
Mowla L. A., et al., 2019, ApJ, 880, 57
Muzzin A., et al., 2013a, ApJS, 206, 8
Muzzin A., et al., 2013b, ApJ, 777, 18
Naab T., Johansson P. H., Ostriker J. P., 2009, ApJ, 699, L178
Oogi T., Habe A., 2013, MNRAS, 428, 641
Oser L., Naab T., Ostriker J. P., Johansson P. H., 2012, ApJ, 744, 63
Osterbrock D. E., Ferland G. J., 2006, Astrophysics of gaseous nebulae and active galactic nuclei. University Science Books
Owers M. S., et al., 2017, MNRAS, 468, 1824
Ownsworth J. R., Conselice C. J., Mortlock A., Hartley W. G., Almaini O., Duncan K., Mundy C. J., 2014, MNRAS, 445, 2198
Peng C. Y., Ho L. C., Impey C. D., Rix H.-W., 2010, AJ, 139, 2097
Perez F., Granger B. E., 2007, Computing in Science Engineering, 9, 21
Pezzulli G., Fraternali F., Boissier S., Muñoz-Mateos J. C., 2015, MNRAS, 451, 2324
Pietrinferni A., Cassisi S., Salaris M., Castelli F., 2004, ApJ, 612, 168
Pietrinferni A., Cassisi S., Salaris M., Castelli F., 2006, ApJ, 642, 797
Pillepich A., et al., 2018, MNRAS, 475, 648
Ravindranath S., et al., 2004, ApJ, 604, L9
Renzini A., Peng Y.-j., 2015, ApJ, 801, L29
Sánchez-Blázquez P., et al., 2006, MNRAS, 371, 703
Scott N., et al., 2009, MNRAS, 398, 1835
Scott N., et al., 2017, MNRAS, 472, 2833
Scott N., et al., 2018, MNRAS, 481, 2299
Scoville N., et al., 2007, ApJS, 172, 38
Sersic J. L., 1968, Atlas de Galaxias Australes. Observatorio Astronomico, Universidad Nacional de Cordoba
Sharp R., et al., 2006, in Society of Photo-Optical Instrumentation Engineers (SPIE) Conference Series. p. 62690G (arXiv:astro-ph/0606137), doi:10.1117/12.671022
Sharp R., et al., 2015, MNRAS, 446, 1551
Speagle J. S., Steinhardt C. L., Capak P. L., Silverman J. D., 2014, ApJS, 214, 15
Storn R., Price K., 1997, Journal of Global Optimization, 11, 341
Stott J. P., et al., 2016, MNRAS, 457, 1888
Straatman C. M. S., et al., 2018, ApJS, 239, 27
Swinbank A. M., Smail I., Sobral D., Theuns T., Best P. N., Geach J. E., 2012, ApJ, 760, 130
Tacconi L. J., et al., 2010, Nature, 463, 781
Tacconi L. J., et al., 2013, ApJ, 768, 74
Taylor M. B., 2005, in Shopbell P., Britton M., Ebert R., eds, Astronomical Society of the Pacific Conference Series Vol. 347, Astronomical Data Analysis Software and Systems XIV. p. 29
Thomas D., Maraston C., Schawinski K., Sarzi M., Silk J., 2010, MNRAS, 404, 1775
Trager S. C., Faber S. M., Worthey G., González J. J., 2000, AJ, 120, 165
Trujillo I., et al., 2006, ApJ, 650, 18
Trujillo I., Conselice C. J., Bundy K., Cooper M. C., Eisenhardt P., Ellis R. S., 2007, MNRAS, 382, 109
Van Rossum G., Drake Jr F. L., 1995, Python reference manual. Centrum voor Wiskunde en Informatica Amsterdam
Vazdekis A., Koleva M., Ricciardelli E., Röck B., Falcón-Barroso J., 2016, MNRAS, 463, 3409
Virtanen P., et al., 2020, Nature Methods, 17, 261
Vogelsberger M., et al., 2014, MNRAS, 444, 1518
Wake D. A., van Dokkum P. G., Franx M., 2012, ApJ, 751, L44
Weiner B. J., et al., 2006, ApJ, 653, 1027
Wellons S., et al., 2015, MNRAS, 449, 361
Whitaker K. E., van Dokkum P. G., Brammer G., Franx M., 2012, ApJ, 754, L29
Whitaker K. E., et al., 2017, ApJ, 838, 19
Williams R. J., Quadri R. F., Franx M., van Dokkum P., Toft S., Kriek M., Labbé I., 2010, ApJ, 713, 738
Wisnioski E., et al., 2011, MNRAS, 417, 2601
Wisnioski E., et al., 2015, ApJ, 799, 209
Wisnioski E., et al., 2019, ApJ, 886, 124
Worthey G., Faber S. M., Gonzalez J. J., 1992, ApJ, 398, 69
Wright E. L., 2006, PASP, 118, 1711
Wright S. A., Larkin J. E., Law D. R., Steidel C. C., Shapley A. E., Erb D. K., 2009, ApJ, 699, 421
Wu P.-F., et al., 2018, ApJ, 868, 37
Wu P.-F., et al., 2020, ApJ, 888, 77
Wuyts S., et al., 2011, ApJ, 742, 96
Yano M., Kriek M., van der Wel A., Whitaker K. E., 2016, ApJ, 817, L21
Zibetti S., Gallazzi A. R., Hirschmann M., Consolandi G., Falcón-Barroso J., van de Ven G., Lyubenova M., 2020, MNRAS, 491, 3562
Zolotov A., et al., 2015, MNRAS, 450, 2327
da Cunha E., Charlot S., Elbaz D., 2008, MNRAS, 388, 1595
de Graaff A., et al., 2020, ApJ, 903, L30
de Graaff A., et al., 2021, arXiv e-prints, p. arXiv:2103.12753
van Dokkum P. G., Franx M., 2001, ApJ, 553, 90
van Dokkum P. G., et al., 2010, ApJ, 709, 1018
van Dokkum P. G., et al., 2015, ApJ, 813, 23
van de Sande J., et al., 2021, MNRAS, 505, 3078
van der Walt S., Colbert S. C., Varoquaux G., 2011, Computing in Science Engineering, 13, 22
van der Wel A., Bell E. F., van den Bosch F. C., Gallazzi A., Rix H.-W., 2009, ApJ, 698, 1232
van der Wel A., et al., 2012, ApJS, 203, 24
van der Wel A., et al., 2014, ApJ, 788, 28
van der Wel A., et al., 2016, ApJS, 223, 29
van der Wel A., et al., 2021, arXiv e-prints, p. arXiv:2108.00744

This paper has been typeset from a TEX/LATEX file prepared by the author.